

Exploring Structural Sparsity of Coil Images from 3-Dimensional Directional Tight Framelets for SENSE Reconstruction*

Yanran Li[†], Raymond H. Chan[‡], Lixin Shen[§], Xiaosheng Zhuang[¶], Risheng Wu[†],
Yijun Huang[†], and Junwei Liu[†]

Abstract. Each coil image in a parallel magnetic resonance imaging (pMRI) system is an imaging slice modulated by the corresponding coil sensitivity. These coil images, structurally similar to each other, are stacked together as 3-dimensional (3D) image data, and their sparsity property can be explored via 3D directional Haar tight framelets. The features of the 3D image data from the 3D framelet systems are utilized to regularize sensitivity encoding (SENSE) pMRI reconstruction. Accordingly, a so-called SENSE3d algorithm is proposed to reconstruct images of high quality from the sampled K -space data with a high acceleration rate by decoupling effects of the desired image (slice) and sensitivity maps. Since both the imaging slice and sensitivity maps are unknown, this algorithm repeatedly performs a slice step followed by a sensitivity step by using updated estimations of the desired image and the sensitivity maps. In the slice step, for the given sensitivity maps, the estimation of the desired image is viewed as the solution to a convex optimization problem regularized by the sparsity of its 3D framelet coefficients of coil images. This optimization problem, involving data from the complex field, is solved by a primal-dual three-operator splitting (PD3O) method. In the sensitivity step, the estimation of sensitivity maps is modeled as the solution to a Tikhonov-type optimization problem that favors the smoothness of the sensitivity maps. This corresponding problem is nonconvex and could be solved by a forward-backward splitting method. Experiments on real phantoms and *in vivo* data show that the proposed SENSE3d algorithm can explore the sparsity property of the imaging slices and efficiently produce reconstructed images of high quality with reduced aliasing artifacts caused by high acceleration rate, additive noise, and the inaccurate estimation of each coil sensitivity. To provide a comprehensive picture of the overall performance of our SENSE3d model, we provide the quantitative index (HaarPSI) and comparisons to some deep learning methods such as VarNet and fastMRI-UNet.

Key words. pMRI and SENSE, structural sparsity, directional Haar framelet regularization, 3D features, PD3O, HaarPSI, U-Net, VarNet, fastMRI-UNet

*Received by the editors May 8, 2023; accepted for publication (in revised form) January 29, 2024; published electronically April 11, 2024.

<https://doi.org/10.1137/23M1571150>

Funding: The work of first author was supported in part by Shenzhen Science and Technology Program (grant JCYJ 20230808105610021). The work of second author was supported in part by HKRGC grants CUHK14301718, NCityU214/19, CityU11301120, CityU11309922, C1013-21GF, and CityUGrant9380101. The work of third author was supported in part by the National Science Foundation under grants DMS-1913039 and DMS-2208385, and Syracuse CUSE grant. The work of forth author was supported in part by the Research Grants Council of Hong Kong (projects CityU 11309122 and CityU 11302023).

[†]College of Computer Science and Software Engineering, Guangdong Key Laboratory of Intelligent Information Processing and Shenzhen Key Laboratory of Media Security, Shenzhen University, Shenzhen 518060 China (lyran@szu.edu.cn, sunrise_wu@foxmail.com, 2070276106@email.szu.edu.cn, 2200271023@email.szu.edu.cn).

[‡]Department of Mathematics, City University of Hong Kong, Kowloon Tong, Hong Kong SAR 999077 China and Hong Kong Centre for Cerebro-Cardiovascular Health Engineering, Hong Kong Science Park, 999077 Hong Kong (raymond.chan@cityu.edu.hk).

[§]Department of Mathematics, Syracuse University, Syracuse, NY 13244 USA (lshen03@syr.edu).

[¶]Department of Mathematics, City University of Hong Kong, Kowloon Tong, 999077 Hong Kong (xzhuang7@cityu.edu.hk).

MSC codes. 42C15, 42C40, 58C35, 65D18, 65D32

DOI. 10.1137/23M1571150

1. Introduction and motivation. Magnetic resonance imaging (MRI) is a common technique in medical diagnosis. Most of the MRI sequences in use today are based on a “spin-warp” imaging scheme [7], where the spatial information with phase was encoded successively by varying the amplitude of the gradients of the radio frequency pulses. Such a scheme is a Fourier-transform MRI method that produces data in the spatial frequency space, known as the *K-space*. The spatial frequency domain content of the imaged object is encoded directly into $g(k_x, k_y)$, the magnetic resonance (MR) signal at spatial frequencies k_x and k_y in the x - and y -directions, respectively. In the *K*-space of the form $g(k_x, k_y) = \iint s(x, y)u(x, y)e^{2\pi i x k_x}e^{2\pi i y k_y} dx dy$, $s(x, y)$ is the *coil sensitivity function* and $u(x, y)$ is the *spatial spin density function* of the original object such as bones, joints, and soft tissues. The decoding process involves an inverse Fourier transform to obtain the target MRI image $u(x, y)$ for medical diagnosis purpose. In order to reproduce accurate reconstruction images, enough phase-encoding steps are needed to cover sufficient positions in the *K*-space. Hence, MRI scans typically take longer time.

The parallel MRI (pMRI) technique is a hardware solution used in clinical applications to shorten the imaging time. It utilizes a set of receiver coils surrounding the target object to detect MR signals. To accelerate the data acquisition procedure, the pMRI system uses reconstruction algorithms to predict the imaging structures of the original MR signal only from collected partial (downsampling) *K*-space data [9, 28]. This downsampling process significantly reduces the scan time, but the resulting pMRI reconstruction is ill-posed and requires regularization techniques to improve the quality of the MRI images [6]. Most pMRI techniques can be categorized as the image domain methods (e.g., sensitivity encoding (SENSE)), the *K*-space methods (e.g., generalized autocalibrating partially parallel acquisitions (GRAPPA)), and their hybrids. In this paper, we focus on the SENSE-based pMRI method.

1.1. SENSE-based pMRI reconstruction. SENSE is a technique that allows a reduction in scan time through the use of multiple receiver coils in an imaging mode [28]. More precisely, in a pMRI process, we denote g_ℓ , the acquired *K*-space signal received by the ℓ th coil, by

$$(1.1) \quad g_\ell = PF(s_\ell \odot u) + \eta_\ell, \quad \ell = 1, \dots, L,$$

where L is the total number of coils, $u \in \mathbb{R}^n$ is the vectorization form of the desired image representing the density of the hydrogen protons in tissues (this is for convenience of presentation; in practice, u is kept as a 2D image), $F \in \mathbb{C}^{n \times n}$ is the discrete Fourier transform matrix, $P \in \mathbb{R}^{n \times n}$ is a sampling matrix, $\eta_\ell \in \mathbb{C}^n$ is the additive noise, and $s_\ell \in \mathbb{C}^n$ is the sensitivity vector of the ℓ th coil. Here, $a \odot b$ is the Hadamard product of a and b with the same dimension. The sampling matrix P is diagonal with diagonal entries being 0 or 1. The observation model in (1.1) shows that the coils simultaneously measure the same region but with a downsampling process in order to increase the scan speed.

When the sensitivity vectors s_ℓ are available, we can write (1.1) in a compact form. To this end, let us define $S_\ell := \text{diag}(s_\ell)$ for $\ell = 1, \dots, L$ and

$$(1.2) \quad g := \begin{bmatrix} g_1 \\ \vdots \\ g_L \end{bmatrix}, S := \begin{bmatrix} S_1 \\ \vdots \\ S_L \end{bmatrix}, \eta := \begin{bmatrix} \eta_1 \\ \vdots \\ \eta_L \end{bmatrix}, M := \begin{bmatrix} PFS_1 \\ \vdots \\ PFS_L \end{bmatrix}.$$

With these notations, a unified representation of the acquired signal g_ℓ in (1.1) is given by

$$(1.3) \quad g = Mu + \eta,$$

where $g \in \mathbb{C}^{Ln}$, $M \in \mathbb{C}^{Ln \times n}$, and $\eta \in \mathbb{C}^{Ln}$.

Regularization techniques are often adopted to regularize the ill-posed problem (1.3). In what follows, we address the issues related to dealing with the inverse problem (1.3).

1.2. Structural sparsity of coil images explored via 3D directional framelets. Regularization techniques on the 2D target image are commonly used for SENSE methods to improve the reconstruction quality. One typical example is the framelet (or wavelet) regularization model of the following form:

$$(1.4) \quad \min \left\{ \frac{1}{2} \|Mu - g\|_2^2 + \|\Gamma W_{2D} u\|_1 : u \in \mathbb{R}^n \right\},$$

where Γ is a diagonal matrix with nonnegative diagonal elements and W_{2D} is the matrix associated with a 2D framelet transform. Model (1.4) uses fixed (pre-estimated) coil sensitivity maps s_ℓ and regularizes on the framelet coefficients of the underlying target image u . It applies W_{2D} on each coil image or target slice to produce sparse coefficient sequences and process them one by one. We refer to (1.4) as the *SENSE2d-U model*.

The pMRI system has multiple coil images, and each coil image contains parts of the information of the target slice that are correlated with each other. For example, Figure 1(a) shows the four coil images of size 512×512 from (the inverse discrete Fourier transform of) the corresponding full K -space data g_ℓ acquired by an MRI machine. It can be seen that the intensity of each coil image is uneven and the intensities of the coil images are mismatched. Without considering their correlated information together, it could lead to poor quality of the reconstruction image; e.g., see Figure 2(c).

Observe that the coil images are sparse in two aspects: (1) Each coil image contains essentially smooth areas separated by edge features, and (2) the coil images are structurally similar to each others with areas of different high intensity. How can we explore the sparsity within each coil image and among different coil images? In view of the fact that the coil images are from the same target slice modulated via multiple coils in different positions, it is thus natural and reasonable to stack and view them as a 3D signal (data) of size $512 \times 512 \times 4$; see Figure 1(b). We can then use a 3D directional framelet system to get a more harmonic image and explore its sparsity. More precisely, using a 3D Haar lowpass filter a^H in a 3D directional Haar framelet (DHF) system $\text{DHF}_3^3 = \{a^H; b_x, b_y, b_{xy}, b_{x,y}, b_{aux}\}$ (see section 2) that plays the role of averaging, the neighboring coil images with labels (1)–(4) are averaged, which produces a 3D signal of four images, labeled as (1 + 2), (2 + 3), (3 + 4), and (4 + 1), having more areas

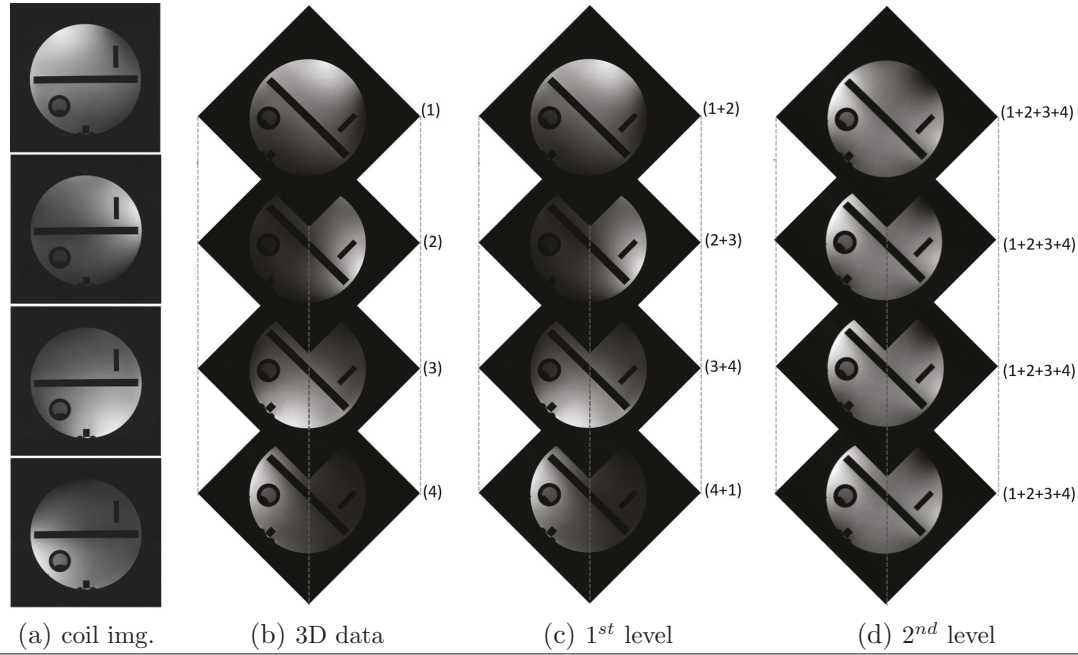


Figure 1. 2-Level 3D directional Haar tight framelet lowpass filtering. (a) Four 512×512 coil images. (b) The 4 coil images, labeled as (1), (2), (3), and (4), are stacked as 3D image data of size $512 \times 512 \times 4$. (c) First-level lowpass filtering of the 3D image by a 3D Haar lowpass filter a^H . This results in images obtained from averaging within each coil image and across coil images. (d) Second-level lowpass filtering of the middle 3D image. Each slice of the second-level filtered 3D image is the same, which is the average of the 4 coil images.

with less intensive difference; see Figure 1(c). In the second level, the 3D signal, which is the stacked version of the four images $(1 + 2)$, $(2 + 3)$, $(3 + 4)$, and $(4 + 1)$, is further averaged by the upsampled lowpass filter, which produces a 3D signal of four images with label $(1 + 2 + 3 + 4)$ having almost the same intensity level of brightness (see Figure 1(d)). The lowpass filtering by the 3D tight framelet filter greatly utilizes the correlated information among the coil images as well as within-the-coil images to produce images with harmonic intensity level, which, in turn, facilitates the production of the sparse representation of the 3D signal by the directional highpass filters $b_x, b_y, b_{xy}, b_{x,y}$ (playing the role of differencing) of the 3D framelet system DHF_3^3 . The full 3D directional framelet system DHF_3^3 plays the central role in our 3D SENSE-based pMRI regularization model.

In view of the above discussion, it is natural to consider the following 3D framelet regularization pMRI model:

$$(1.5) \quad \min \left\{ \frac{1}{2} \|Mu - g\|_2^2 + \|\Gamma W_{3D} S u\|_1 : u \in \mathbb{R}^n \right\},$$

where W_{3D} is the matrix associated with a 3D tight framelet transform. The differences of the regularization terms in (1.4) and (1.5) are obvious. The regularization term $\|\Gamma W_{2D} u\|_1$ in

(1.4) measures the sparsity with the ℓ_1 norm for the desired image u under a 2D tight framelet transform, while the regularization term $\|\Gamma W_{3D} S u\|_1$ in (1.5), as motivated by Figure 1(c), measures the sparsity with the ℓ_1 norm of all coil images $S u$ under a 3D framelet transform. If S is pre-estimated, then we shall call such a model in (1.5) the *SENSE3d-U model*.

1.3. The SENSE3d algorithm and the SENSE3d model. The sensitivity vectors s_ℓ are spatially nonuniform and are unknown. The difficulty of model (1.5) is to find an estimate of u under the scenario that s_ℓ are unknown and the acquired K -space signals g_ℓ are incomplete. For the SENSE2d-U model and SENSE3d-U models, each sensitivity map s_ℓ is usually pre-estimated as follows: The blurry coil image $\tilde{g}_\ell = F^{-1} g_\ell$ is acquired by the inverse Fourier transform of the center K -space data, and then, the sensitivity for each coil is estimated as $s_\ell = \tilde{g}_\ell / \sqrt{|\tilde{g}_1|^2 + \dots + |\tilde{g}_L|^2}$. However, both models with such pre-estimated coil selectivity maps usually do not perform well. See Figure 2(c), (d), and (e).

We treat both u and the sensitivity vectors s_ℓ as our *target solutions* in our proposed optimization models and propose a so-called SENSE3d algorithm to find the estimates of u and s_ℓ iteratively. The basic steps in the SENSE3d algorithm are the ‘slice step’ and the ‘sensitivity step’:

- (1) Slice step: Find an estimate of the slice image u from the observed K -space signals g_ℓ and the guesses of s_ℓ . The reconstruction of u from (1.3) is obtained by solving an optimization model (see (1.5) or (3.3)) regularized by a 3D directional Haar tight framelet system.
- (2) Sensitivity step: Update the sensitivity vectors s_ℓ for $\ell = 1, 2, \dots, L$ from the observed K -space signal g_ℓ and the estimate of u . The target image u is obtained by using

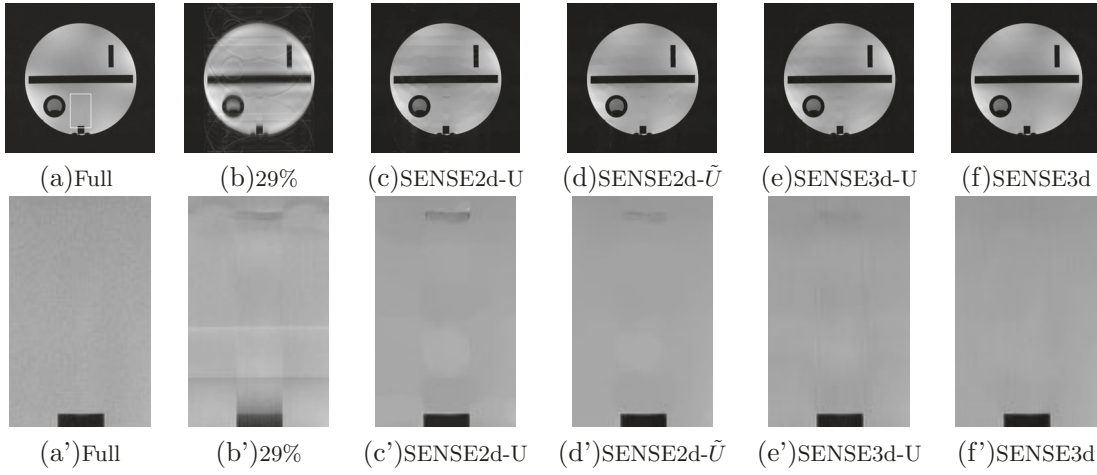


Figure 2. (a) Reference *Sum of Square (SoS)* image by the full K -space data with to-be zoomed-in area (the white rectangle); (b) *SoS* image by the four coil images with 29% K -space data on uniform sampling model as shown in Figure 3(a); (c) the SENSE2d-U model (1.4) by pMRI algorithm *Fast Adaptive Directional Haar Framelet Algorithm (FADHFA)* [21]; (d) the SENSE2d- \tilde{U} , which is the pMRI algorithm *FADHFA* using the sensitivity map estimated by our SENSE3d algorithm; (e) the SENSE3d-U model (1.5); and (f) the SENSE3d model (3.3) + (3.10). (a')–(f'): The zoomed-in part of (a)–(f) of the same white rectangle area, respectively.

a smooth assumption on s_ℓ . Once we have an approximation to the target image u , we can use it to update the sensitivities that are the solution of a Tikhonov-type optimization model (see (3.10)).

The above two steps are alternately repeated until stability is reached. To avoid additional notation, details on the slice step and the sensitivity step will be discussed in section 3. We shall call the model using the SENSE3d algorithm—that is, (3.3) and (3.10) detailed in section 3 together with our DHF₃³ framelet regularization—the *SENSE3d model*.

The SENSE3d model significantly improves the quality of the reconstruction target image u . One can see the performance comparisons among the four models SENSE2d-U, SENSE3d-U, SENSE3d, and SENSE2d- \tilde{U} , from Figure 2. We use phantom images with four coil images of size 512×512 . The K -space data of each coil are partially sampled according to the sampling model in Figure 3(a) (29% of the K -space with 24 autocalibration signal (ACS) lines). Figure 2(b) is the SoS (sum-of-square) image of the four downsampled coil images, which is obviously blurred with aliasing artifacts. The MRI images reconstructed by SENSE2d-U, SENSE2d- \tilde{U} , SENSE3d-U, and SENSE3d are shown in Figure 2(c), (d), (e), and (f), respectively.

Comparing the SENSE3d-U and SENSE2d-U models, one can see that SENSE3d-U model is better in reducing the aliasing artifacts than that of the SENSE2d-U model. As shown by the zoomed-in parts, the “Column” and the “Row” aliasing artifacts in Figure 2(c) (SENSE2d-U) are mostly reduced by the SENSE3d-U model in Figure 2(e'). This confirms that the correlated futures of coil images by our 3D framelet system can efficiently suppress the artifacts by the downsampling operation in the K -space domain. Comparing the SENSE3d-U model (without iterating updates of s_ℓ) and the SENSE3d model (with iterating updating of s_ℓ), one can see from Figure 2(e) and (f) that the reconstruction target image u by the SENSE3d does not have aliasing artifacts. The zoomed-in parts in Figure 2(e') and (f') show that the SENSE3d model can get more accurate sensitivity to reconstruct better target images. Aliasing artifacts in Figure 2(e') are removed in Figure 2(f') via our SENSE3d models. Finally, the SENSE2d- \tilde{U} , which is the pMRI algorithm FADHFA using the sensitivity map estimated by our SENSE3d algorithm, shows its improvement over SENSE2d-U but is still not as good as SENSE3d-U.

The performance of the SENSE3d-U model from the above is better than that of the SENSE2d-U model, while the performance of the SENSE3d model is better than that of the SENSE3d-U model. The reconstructed and sensitivity models in (3.3) and (3.10), respectively, interact with each other to improve the quality of the MRI images by our DHF₃³ framelet regularization. We demonstrate in section 4 with more experimental results for comparing with other state-of-the-art methods.

1.4. Contributions and structure. The contributions of the paper mainly lie in the following three aspects. First, we introduce the use of 3D DHFs for the regularization of the pMRI reconstruction under the SENSE-based method. In view of the correlated information among coil images, the 3D DHF system DHF₃³ not only produces coil images with harmonic pixel intensity but also greatly facilitates the exploration of the sparsity within each coil image as well as the sparsity across coil images. Secondly, we propose a so-called SENSE3d algorithm to estimate the target image and the coil sensitivity maps iteratively. Unlike some 2D models

and 3D models that are using pre-estimated coil sensitivity maps, our SENSE3d algorithm treats both the underlying image u and the coil sensitivity maps s_ℓ as our target solutions of some optimization models by 3D regularization. Such a SENSE3d algorithm together with our 3D DHF regularization gives rise to our SENSE3d model, which provides high-quality reconstruction images with excellent performance improvement. Finally, we provide detailed step-by-step procedures for solving the optimization problems appeared in the slice step and sensitivity step of the SENSE3d algorithm. Moreover, we give theoretical justifications on the convergence analysis of the two iterative algorithms for the slice step and sensitivity step, respectively.

The structure of the paper is as follows. In section 2, we discuss 3D DHFs for our pMRI regularization. In section 3, we present our optimization model for the pMRI SENSE reconstruction and develop the numerical algorithms to solve the model iteratively. In section 4, we conduct numerical experiments on the comparisons of several state-of-the-art methods using various MRI data. Conclusions and further remarks are given in the last section. Some proofs are postponed to the appendix.

2. 3D directional Haar framelets filter banks. In what follows, we briefly discuss the 3D directional Haar tight framelet filter bank DHF₃³ for our 3D SENSE-based pMRI regularization model.

By $l_0(\mathbb{Z}^d)$, we denote the set of all finitely supported sequences. A *mask/filter* $h = \{h(k)\}_{k \in \mathbb{Z}^d} : \mathbb{Z}^d \rightarrow \mathbb{C}$ on \mathbb{Z}^d is a sequence in $l_0(\mathbb{Z}^d)$ whose *Fourier series* is defined to be $\hat{h}(\xi) := \sum_{k \in \mathbb{Z}^d} h(k) e^{-ik \cdot \xi}$ for $\xi \in \mathbb{R}^d$. We denote δ as the *Dirac sequence* such that $\delta(0) = 1$ and $\delta(k) = 0$ for all $k \in \mathbb{Z}^d \setminus \{0\}$ and $\delta_\gamma := \delta(\cdot - \gamma)$ for $\gamma \in \mathbb{Z}^d$. Throughout the paper, we assume that the tight framelets are *dyadic dilated*; that is, the *dilation matrix* is $2I_d$, with I_d the $d \times d$ identity matrix. For filters $a, b_1, \dots, b_m \in l_0(\mathbb{Z}^d)$, we say that a filter bank $\{a; b_1, \dots, b_m\}$ is a *(d-dimension dyadic) tight framelet filter bank* if, for all $\xi \in \mathbb{R}^d, \omega \in \{0, 1\}^d$,

$$(2.1) \quad \widehat{a}(\xi) \overline{\widehat{a}(\xi + \pi\omega)} + \sum_{\iota=1}^m \widehat{b}_\iota(\xi) \overline{\widehat{b}_\iota(\xi + \pi\omega)} = \delta(\omega),$$

where \bar{x} denotes the complex conjugate of $x \in \mathbb{C}$. The filter a is a lowpass filter satisfying $\widehat{a}(0) = 1$, while b_ι 's are the highpass filters satisfying $\widehat{b}_\iota(0) = 0$. Such a filter bank $\{a; b_1, \dots, b_m\}$ corresponds to a *framelet system* $\{\varphi; \psi_1, \dots, \psi_m\}$ through the refinement relations $\widehat{\varphi}(2\xi) = \widehat{a}(\xi)\widehat{\varphi}(\xi)$ and $\widehat{\psi}_\iota(2\xi) = \widehat{b}_\iota(\xi)\widehat{\varphi}(\xi)$, where the *Fourier transform* is defined to be $\widehat{f}(\xi) := \int_{\mathbb{R}^d} f(x) e^{-ix \cdot \xi} dx$ for a function $f \in L_1(\mathbb{R}^d)$. For more details, we refer to [11].

Now, consider $a^H = 2^{-d} \sum_{\gamma \in \{0, 1\}^d} \delta_\gamma$ to be the d -dimensional Haar lowpass filter. Define the set $\{b_1, \dots, b_m\} := \{2^{-d}(\delta_{\gamma_1} - \delta_{\gamma_2}) : \gamma_1, \gamma_2 \in \{0, 1\}^d \text{ and } \gamma_1 < \gamma_2\}$ of highpass filters. Here, $\gamma_1 < \gamma_2$ is understood in the sense of lexicographical order. Then, we have $m = \binom{2^d}{2} = 2^{d-1}(2^d - 1)$. It was shown in [12] (see also [19, 38] for the generalization) that $\{a^H; b_1, \dots, b_m\}$ is a tight framelet filter bank such that all the highpass filters b_1, \dots, b_m have only two taps and exhibit $\frac{1}{2}(3^d - 1)$ directions in dimension d . In particular, for $d = 1$, the tight framelet filter bank is just the standard Haar orthogonal wavelet filter bank DHF₁ := $\{a^H; b\}$ with $a^H = \frac{1}{2}(\delta_0 + \delta_1)$ and $b = \frac{1}{2}(\delta_0 - \delta_1)$. For $d = 2$, the corresponding tight framelet filter bank reduces to the directional Haar tight framelet filter bank DHF₂ := $\{a^H; b_1, \dots, b_6\}$ in [21, equation (3.5)].

For $d = 3$, it is a 3D directional Haar tight framelet filter bank $\text{DHF}_3^1 := \{a^H; b_1, \dots, b_{28}\}$ with $a^H = \frac{1}{8}(\delta_{(0,0,0)} + \delta_{(0,0,1)} + \delta_{(0,1,0)} + \delta_{(0,1,1)} + \delta_{(1,0,0)} + \delta_{(1,0,1)} + \delta_{(1,1,0)} + \delta_{(1,1,1)})$ and the 28 filters $b_\ell = \frac{1}{8}(\delta_{\gamma_1^\ell} - \delta_{\gamma_2^\ell})$ for $\ell = 1, \dots, 28$. Since we employ the UDFmTs (undecimated discrete framelet transforms) for the W_{3D} in our model (1.5), only the partition of unity condition is needed ($\omega = 0$ in (2.1)) to guarantee the perfect reconstruction property. Hence, by considering filters with the same direction, the 28 highpass filters in DHF_3^1 can be regrouped to 13 filters as a filter bank DHF_3^2 with filters $a^H, b_x, b_y, b_z, b_{xy}, b_{x,y}, b_{xz}, b_{x,z}, b_{yz}, b_{y,z}, b_{xyz}, b_{xy,z}, b_{x,yz}, b_{xz,y}$ in [23]. Furthermore, as demonstrated in [22], the output framelet coefficient sequences involving the z -filters (i.e., those b_z, b_{xz}, b_{xyz} , etc.) are actually ‘bad’ features for our 3D signal reconstruction. They represent local contrast discrepancy between coil images that do not play a role in our restriction process. Hence, in [22], the filter bank DHF_3^2 is further simplified to the filter bank $\text{DHF}_3^3 := \{a^H; b_x, b_y, b_{xy}, b_{x,y}, b_{aux}\}$, where $b_x = \frac{1}{4}(\delta_{(1,0,0)} - \delta_{(0,0,0)})$, $b_y = \frac{1}{4}(\delta_{(0,1,0)} - \delta_{(0,0,0)})$, $b_{xy} = \frac{\sqrt{2}}{8}(\delta_{(1,1,0)} - \delta_{(0,0,0)})$, and $b_{x,y} = \frac{\sqrt{2}}{8}(\delta_{(1,0,0)} - \delta_{(0,1,0)})$ and the filter b_{aux} is determined by $\widehat{b_{aux}} := 1 - (|a^H|^2 + |\widehat{b_x}|^2 + |\widehat{b_y}|^2 + |\widehat{b_{xy}}|^2 + |\widehat{b_{x,y}}|^2)$.

The 3D directional Haar filter bank DHF_3^3 nicely fits into our SENSE pMRI regularization and reconstruction with the following properties: (a) The lowpass filter a^H produces an underlying image with harmonic pixel intensity for further process by the directional highpass filters; (b) the directional highpass filters $b_x, b_y, b_{xy}, b_{x,y}$ are properly chosen to capture the edge information for the sparse representation, which facilitates the successful recovery in the ℓ_1 -based optimization models; and (c) the auxiliary filter b_{aux} guarantees the perfect reconstruction of the 3D filter bank and the UDFmT, where, in practice, it does not participate in the shrinkage operation so that the procedure of UDFmTs is equivalent to the UDFmT using the tight framelet filter bank DHF_3^2 . We refer to [22, 23] for the detailed construction of the DHF_3^3 and the implementation of the UDFmT based on the DHF_3^3 .

3. Optimization models and the SENSE3d algorithm. The problem (1.1) is highly ill-posed because different pairs of u and s_ℓ can bring about the same g_ℓ . Under the prior knowledge about u and s_ℓ , our goal is to approximate the desired image u when s_ℓ are unknown and the acquired K -space signal g_ℓ are incomplete. To achieve this goal, we introduce a so-called SENSE3d algorithm for finding an estimate of both u and s_ℓ . The basic steps for the SENSE3d algorithm are outlined in Algorithm 3.1.

Algorithm 3.1. The SENSE3d algorithm.

- 1: Given the observed K -space signal g_ℓ , sampling matrix P and an initial sensitivity matrix s_ℓ^0 , $\ell = 1, 2, \dots, L$,
- 2: **for** $k = 1, 2, \dots$, **do**
- 3: slice step: Find an estimate of u from the observed K -space signals g_ℓ and the estimated sensitivity matrices s_ℓ ;
- 4: sensitivity step: Update the sensitivity vectors s_ℓ for $\ell = 1, 2, \dots, L$ from the observed K -space signal g_ℓ and the estimated image u .
- 5: **end for**
- 6: Return u^∞ the estimate of the desired image u .

The SENSE3d algorithm is an iterative way to find the estimate of u by decoupling the effects of u and the sensitivity maps s_ℓ . We remark that a model called JSENSE, which alternatively estimates the slice image u and the sensitivity vectors s_ℓ , was proposed in [44], but it is without considering any regularization technique and the convergence analysis. On the other hand, in the slice step of Algorithm 3.1 for our SENSE3d model, we integrate the regularization with the novel 3D directional Haar filter bank DHF₃³, which captures the sparsity of the coil images. In the sensitivity step of Algorithm 3.1, we propose a Tikhonov-type regularization that favors the smoothness of the sensitivity mapping s_ℓ , $\ell = 1, 2, \dots, L$. For the regularized optimization problems in the slice step and sensitivity step, we develop efficient algorithms to solve them and provide convergence analysis of these algorithms.

3.1. Slice step: Object estimation. We begin by introducing the basic notation. The pMRI acquisition model involves complex numbers. For a vector $u \in \mathbb{C}^n$, we use $\|u\|_2 := \sqrt{\sum_{j=1}^n |u[j]|^2}$, $\|u\|_1 := \sum_{j=1}^n |u[j]|$, and $\|u\|_\infty := \max_{1 \leq j \leq n} |u[j]|$ to represent, respectively, the ℓ_2 -, ℓ_1 -, and ℓ_∞ -norms of u , where $u[j]$ is the j th component of u . For a matrix $A \in \mathbb{C}^{m \times n}$, we define its norm as follows:

$$\|A\|_2 := \max \{ \|Au\|_2 : u \in \mathbb{C}^n \text{ with } \|u\|_2 = 1 \}.$$

Hereafter, $\text{Re}(\cdot)$ and $\text{Im}(\cdot)$ stand for the real and imaginary parts, respectively. For $u \in \mathbb{C}^n$, we have $u = \text{Re}(u) + i\text{Im}(u)$, where both $\text{Re}(u)$ and $\text{Im}(u)$ are in \mathbb{R}^n and i is the imaginary unit satisfying $i^2 = -1$.

For the purpose of the exposition of optimization algorithms on \mathbb{C}^n , the inner product of two vectors u and v in \mathbb{C}^n is defined as

$$(3.1) \quad \langle u, v \rangle := \text{Re}(u^\top v),$$

where u^\top is the conjugate transpose of u . With this inner product, the vector space \mathbb{C}^n is actually viewed as the vector space \mathbb{R}^{2n} .

From the observed K -space signals g_ℓ and the estimated sensitivity maps s_ℓ , we propose to estimate u in (1.1) through an optimization model that is regularized by the prior knowledge of the coil images. Note that the ℓ th coil image $s_\ell \odot u = \text{diag}(s_\ell)u = S_\ell u$. From the identities $S_\ell u = F^{-1}FS_\ell u$ and $I_n = (I_n - P) + P$, in the noise-free situation, we have

$$S_\ell u = F^{-1}((I_n - P)FS_\ell u + PFS_\ell u) = F^{-1}(I_n - P)FS_\ell u + F^{-1}g_\ell$$

for all $\ell = 1, 2, \dots, L$. Putting all L coil images together, the above equations yield

$$(3.2) \quad c = Nu + (I_L \otimes F^{-1})g,$$

where $c = Su$ and $N = (I_L \otimes (F^{-1}(I_n - P)F))S$. Here, S is defined in (1.2) and \otimes denotes the *Kronecker product*. Equation (3.2) says that the integration of the coil images c is composed of the missing information Nu and the available information $(I_L \otimes F^{-1})g$.

Denoting $W := W_{3D}$ as the transformation matrix associated with the filter bank DHF₃³ onto the coil images c , we have $Wc = W(Nu + (I_L \otimes F^{-1})g)$. Using this identity, (1.3), and (3.2), we propose to estimate image u through the following optimization problem:

$$(3.3) \quad \min \left\{ \frac{1}{2} \|Mu - g\|_2^2 + \|\Gamma W(Nu + (I_L \otimes F^{-1})g)\|_1 : u \in \mathbb{R}^n \right\},$$

where Γ is a diagonal matrix with nonnegative diagonal entries. In the objective function of (3.3), the term $\frac{1}{2}\|Mu - g\|_2^2$ measures the faithfulness of the recovered image to the given data, while the term $\|\Gamma W(Nu + (I_L \otimes F^{-1})g)\|_1$ relates to the sparsity of the coil images $Nu + (I_L \otimes F^{-1})g$ under W . Note that the ideal image u is restricted in \mathbb{R}^n .

With the above preparation, we first present the PD3O (primal-dual three-operator splitting) algorithm for solving (3.3) and the convergence analysis of the sequence generated by the algorithm. We postpone discussion on the development and the convergence analysis of the algorithm to Appendix A.1 to avoid a lengthy digression.

This algorithm is written as follows: Given the initial guess $(v^0, z^0) \in \mathbb{C}^n \times \mathbb{C}^d$ and the parameters γ , δ and Γ , iterate

$$\begin{cases} u^k = \text{Re}(v^k), \\ w^k = (I - \gamma\delta AA^\top)z^k + \delta A(\bar{v}^k - \gamma M^\top(Mu^k - g)), \\ z^{k+1} = (w^k + \delta b) - \text{soft}(w^k + \delta b, \Gamma), \\ v^{k+1} = u^k - \gamma M^\top(Mu^k - g) - \gamma A^\top z^{k+1}. \end{cases}$$

Here, $A = WN$, $b = W(I_L \otimes F^{-1})g$, and w^k is the auxiliary variable. Furthermore, soft is the well-known soft shrinkage operator; i.e., for $w \in \mathbb{C}^d$,

$$(\text{soft}(w, \Gamma))[j] = \max\{|w[j]| - \Gamma[j, j], 0\} \frac{w[j]}{|w[j]|}$$

for $j = 1, 2, \dots, d$. One iteration of the above scheme can be viewed as the operator T_{PD3O} (see (A.3a), (A.3b), and (A.3c) in Appendix A.1 for its definition) such that $(v^{k+1}, z^{k+1}) = T_{\text{PD3O}}(v^k, z^k)$.

The theorem for the convergence analysis of the PD3O algorithm for problem (3.3) is given as follows.

Theorem 3.1. *Let the pair (v^*, z^*) be any fixed point of the T_{PD3O} operator. Let κ be defined by*

$$(3.4) \quad \kappa = \max_j \sum_{\ell=1}^L |s_\ell[j]|^2,$$

and let $\{v^k, z^k\}_{k \geq 0}$ be the sequence generated by the PD3O algorithm (A.3a), (A.3b), and (A.3c) with

$$(v^{k+1}, z^{k+1}) = T_{\text{PD3O}}(v^k, z^k)$$

and the initial guess (v^0, z^0) . Choose γ and δ such that $\gamma < 2/\kappa$ and $\gamma\delta < 1/\kappa$. Define $B := \frac{\gamma}{\delta}(I - \gamma\delta AA^\top)$ and $\|(v, z)\|_B := \sqrt{\|v\|^2 + \langle z, Bz \rangle}$. Then, the following statements hold.

- (i) *The sequence $\{\|(v^k, z^k) - (v^*, z^*)\|_B\}_{k \geq 0}$ is monotonically nonincreasing.*
- (ii) *The sequence $\{\|(v^{k+1}, z^{k+1}) - (v^k, z^k)\|_B\}_{k \geq 0}$ is monotonically nonincreasing. Moreover, we have $\|(v^{k+1}, z^{k+1}) - (v^k, z^k)\|_B = o(\frac{1}{k+1})$.*

The detailed proof of the above theorem is given in Appendix A.1. We next focus on the estimation of the sensitivity maps s_ℓ .

3.2. Sensitivity step: Sensitivity maps estimation. Once we have an approximation to the target image u , we can use it to update the sensitivity maps s_ℓ , $\ell = 1, 2, \dots, L$. From the acquisition model (1.1) and the facts that $I_n = P + (I_n - P)$ and $g_\ell = PF(s_\ell \odot u)$ in the noise-free case, the approximation of the full K -space signal, denoted by $g_{est,\ell}$ and received by the ℓ th coil, can be modeled as

$$(3.5) \quad g_{est,\ell} = g_\ell + (I_n - P)F(s_\ell \odot u).$$

That is, $g_{est,\ell}$ is composed of the observed partial K -space information g_ℓ and the estimated unobservable K -space data $(I - P)F(s_\ell \odot u)$. In the noise-free case, due to $s_\ell \odot u = u \odot s_\ell = \text{diag}(u)s_\ell$, we indeed have

$$(3.6) \quad g_{est,\ell} = F(s_\ell \odot u) = (F\text{diag}(u))s_\ell.$$

Define

$$(3.7) \quad g_{est} = \begin{bmatrix} g_{est,1} \\ \vdots \\ g_{est,L} \end{bmatrix}, Q = I_L \otimes (F\text{diag}(u)), s = \begin{bmatrix} s_1 \\ \vdots \\ s_L \end{bmatrix}.$$

Here, $g_{est} \in \mathbb{C}^{Ln}$, $Q \in \mathbb{C}^{Ln \times Ln}$, and $s \in \mathbb{C}^{Ln}$. With these preparations, a compact representation of (3.6) is as follows:

$$(3.8) \quad g_{est} = Qs.$$

To estimate a faithful s from model (3.8), we should take both reliable K -space data information from g_{est} and prior knowledge of s into consideration. Regarding the prior knowledge of s , each sensitivity map s_ℓ is assumed to be smooth and the energy of the values coming from the same location of the sensitivity maps is identical and equal to one; that is, $\sum_{\ell=1}^L |s_\ell[j]|^2 = 1$ for all $j = 1, \dots, n$ (see [24]). Due to $u \odot s_\ell = (hs_\ell) \odot (u/h)$ holding for any nonzero constant h , the constraint on the sensitivity maps s_ℓ ensures the uniqueness of the underlying problem. Therefore, we define the domain

$$(3.9) \quad D := \left\{ s : s \in \mathbb{C}^{Ln}, \sum_{\ell=1}^L |s[j + (\ell - 1)n]|^2 = 1 \text{ for } j = 1, \dots, n \right\}.$$

With these preparations, our proposed optimization problem for estimating s from model (3.8) has a form of

$$(3.10) \quad \min \left\{ \frac{1}{2} \|P_{sel}(Qs - g_{est})\|_2^2 + \frac{1}{2} \|\Gamma_s W s\|_2^2 : s \in D \right\},$$

where P_{sel} is a sampling matrix and $W = W_{3D}$ is associated with the 3D DHF transform used in the slice step. Here, Γ_s is a diagonal matrix whose diagonal entries corresponding to the framelet coefficients from the lowpass filter of the framelet system are zero, and the others have the same value. The use of P_{sel} here is twofold. First, the K -space data are usually fully sampled near its center (i.e., the ACS lines) and thus give more accurate estimation of g_{est}

near the center. The sampling matrix P_{sel} is hence defined to sample coefficients near the center of K -space only. Second, the smooth assumption on each s_ℓ implies that the frequency response of s_ℓ is concentrated around the center of the K -space (a lowpassed signal). Therefore, there is no need to use the full K -space data. Moreover, P_{sel} reduces the computation cost significantly. In our experiments, P_{sel} is indeed the sampling matrix corresponding to the ACS line.

Since the objective function of the optimization problem (3.10) is Lipschitz continuous, problem (3.10) can be solved through the forward-backward algorithm (see, for example, [1]). It reads as, for any initial guess s^0 , iterate

$$(3.11) \quad s^{k+1} = \text{proj}_D(s^k - \tau_k(Q^\top P_{sel}(Qs^k - g_{est}) + W^\top \Gamma^2 W s^k)),$$

where $\tau_k > 0$. Here, if $t = \text{proj}_D(s)$ for $s \in \mathbb{C}^{Ln}$, then, for each $j = 1, 2, \dots, n$, letting $\tilde{t} = [t[j], t[j+n], \dots, t[j+(L-1)n]]$ and $\tilde{s} = [s[k], s[k+n], \dots, s[k+(L-1)n]]$, we have

$$\tilde{t} = \begin{cases} \frac{\tilde{s}}{\|\tilde{s}\|_2} & \text{if } \|\tilde{s}\|_2 \neq 0; \\ \text{any unit-vector in } \mathbb{C}^L, & \text{otherwise.} \end{cases}$$

The convergence analysis of the iterative scheme (3.11) is given in the following theorem.

Theorem 3.2. *Given an $\epsilon \in (0, \frac{1}{2(\|u\|_\infty^2 + \|\text{diag}(\Gamma)\|_\infty^2)})$ and a sequence of stepsize τ_k such that $\epsilon < \tau_k < \frac{1}{\|u\|_\infty^2 + \|\text{diag}(\Gamma)\|_\infty^2} - \epsilon$, we consider the sequence $\{s^k\}_{k \geq 0}$ generated by (3.11). Then, the sequence converges to a point s^* in D such that*

$$Q^\top P_{sel}(Qs^* - g_{est}) + Q^\top \Gamma^2 Qs^* + \nu \text{diag}(I_L \otimes \nu)s^* = 0$$

for some vector $\nu \in \mathbb{R}^n$ with positive $\nu_i \geq 0$, $i = 1, 2, \dots, n$.

The proof of the above theorem is given in Appendix A.2.

4. Experiments. In this section, we provide numerical experiments to demonstrate the performance of our SENSE3d model. We begin by reviewing some related work on SENSE and GRAPPA. We then provide numerical experiments for the comparisons of our model with some traditional methods as well as some deep learning methods.

4.1. Related work. For the SENSE method, total variation (TV) is one of the regularization techniques that has an ability to recover the edge details in the target image for the pMRI problem [43]. It is well known that TV does not distinguish between jumps and smooth transitions and tends to give piecewise constant images with staircase artifacts. Total generalized variation (TGV) with a high-order differential operator can remove the staircase artifacts caused by TV, and the TGV of second order is applied to parallel imaging in [17]. Wavelet transforms are adopted to detect artifacts appearing in the basic SENSE reconstruction and reduce the artifacts by emphasizing the sparse representation of the underlying image [4]. However, the reconstructed image will suffer from ringing artifacts when the wavelet coefficients are modified in an incorrect way. The 2D DHF-based regularization technique assimilating the advantages of both total variation and wavelet regularization, called FADHFA, was proposed for SENSE to preserve details of slice and remove noise in [21]. To adaptively represent the image with sparse canonical coefficients by tight frame, a data-driven tight

frame-based off-the-grid regularization model was proposed for the compressive sensing MRI reconstruction in [3]. The nonconvex and nonsmooth Euler's elastica functional was proposed to regularize SENSE reconstruction in [42]. These 2D regularization techniques only focus on each coil image independently, and the redundant information among multicoil images of pMRI is not considered in the SENSE reconstructions.

The GRAPPA in [9] is a K -space method and interpolates the missing data in the K -space for each coil from the multicoil neighboring K -space samples. The GRAPPA method can reconstruct almost the same quality of images as those from the SENSE method [2], but it requires the ACS data, near the center of K -space, to estimate the interpolation weights or coil sensitivities. In [37], sparsity-promoting calibration was proposed to regularize the GRAPPA-based interpolation weights for reconstructing high-quality MRI images. By exploiting the nonlinear relationship between ACS and missing data, a kernel-based approach was suggested to interpolate the missing data in the K -space [25]. Iterative self-consistent parallel imaging reconstruction (SPIRiT) extends the GRAPPA's interpolation weights on sampled and unsampled data and fills missing K -space as an inverse problem [24]. ESPIRiT is a “soft” SENSE reconstruction using the eigenvectors of a calibration matrix constructed by the SPIRiT model as sensitivity maps and is called ℓ_1 -ESPIRiT by regularizing the wavelet coefficients of the target images with the ℓ_1 -norm [33]. Joint sparsity of the wavelet coefficients of each coil image at same position is applied to the SPIRiT model (ℓ_1 -SPIRiT) [27] and SENSE model (JSCSSENSE) [5] to further improve the quality of the reconstruction results. Since ESPIRiT does not consider the phase of image, an algorithm called VCC-ESPIRiT [34], incorporating the virtual conjugate coils, was proposed to estimate the sensitivity maps that include the absolute phase of the image. A 3D directional Haar tight framelet (3DHF) was proposed to regularize the related features between coil images reconstructed by SPIRiT model for reducing the aliasing artifacts caused by the downsampling operation [23].

The filling of K -space data was formulated as the low-rank matrix completion problem in [14]. The low-rank matrix modeling of local K -space neighborhoods (LORAKS) [10], and simultaneous autocalibration and K -space estimation (SAKE) [31] use local neighborhoods of multicoil K -space data to construct low-rank matrices for regularizing parallel imaging reconstruction. Under smooth-phase assumptions, the LORAKS method also imposes phase constraints on low-rank matrices. When an image is with the finite rate of innovation, then its K -space data have a property with low-ranked weighted Hankel structured matrix, leading to an annihilating filter-based low-rank Hankel matrix approach (ALOHA) [15]. Jointing sparsity of the patches from multicoil images using a sparse dictionary was proposed to regularize the reconstruction coil MR images by considering the cross-channel relationships in [36].

Deep learning methods based on many neural network architectures can discover the internal relationship of large-scale data through training and learning and make multilevel abstract representations of data [40, 41]. A deep convolutional neural network was proposed to learn the regularization part of the optimization model for an inverse problem and was applied to the pMRI problem in [16]. U-Net is a commonly used neural network model in medical image processing [30] and has been successfully applied to MRI reconstruction [32, 45]. An end-to-end variation network (VarNet) [32] is a more powerful model built upon the fastMRI-UNet model [45]. The VarNet model utilizes a sensitivity map estimation module, a refinement module, and a data consistency module to estimate missing K -space data and

reconstruct MRI images. It achieves good results on the fastMRI data set and served as the baseline model for the 2020 fastMRI challenge [26].

Deep learning methods for pMRI reconstruction require a large amount of multicoil K -space data and accurate information about the MR machine acquisitions; however, the parameters of the imaging setting of an MRI machine (for example, field of view, slice thicknesses, and others) may be different for different cases. For example, a person's heartbeat, slight body jitter, and other factors in the process of scanning can form gradient information similar to adversarial attack, which affects the accuracy of prediction and results in blurred anatomical structure details and artifacts in reconstructed MRI images using deep learning methods [8]. Hence, in this paper, we focus on approaches without the need of large-scale data but simply with the small given multicoil data in the pMRI reconstruction. Nevertheless, we provide comparisons of our methods with the deep learning methods as well.

4.2. Parameter settings. The parameter setting of our SENSE3d algorithm is as follows. In the slice step, for the parameters $\gamma = 1.99$ and $\delta = 0.5$, and, for a more precise choice of Γ and the thresholding parameter λ , we refer to [22, section 4.2]; in the sensitivity step, all nonzero diagonal entries of the diagonal matrix Γ are identical, say, each s th diagonal entry $\lambda_s = 0.05$ for all experiments. After this parameter is determined, we choose $\tau_k = \frac{0.99}{2(\|u\|_\infty^2 + \lambda_s^2)}$ and 25 iterations for the sensitivity step. We terminate our method when $\|u^{k+1} - u^k\|_2^2 / \|u^k\|_2^2 < 10^{-6}$ or when the number of iterations exceeds 40. Here, u^k is the k th iteration produced by the underlying algorithm. Our SENSE3d algorithm only updates the sensitivity maps at $k = 8, 16$, and 24 by the sensitivity step and then fixes them after $k = 24$ to guarantee convergence in the slice step. The two-level decomposition of DHF³ is adopted in all experiments.

Several state-of-the-art methods reviewed above, including the fast adaptive DHF algorithm FADHFA [21], the ℓ_1 -ESPIRiT method [33], and ALOHA [15], are adopted to further compare with our SENSE3d model in numerical experiments. The source code of the ℓ_1 -ESPIRiT method was downloaded from the website of Michael Lustig,¹ and its default settings are used except for kernel size with 5×5 , maximal iteration 50, and regularization parameter λ set by hand for its best performance. The source code of the ALOHA method is available at the website of BioImaging, Signal Processing & Learning Lab @ KAIST AI,² and its default settings are used except for the following: pyramidal decomposition with decreasing Low-Rank Matrix Fitting (LMaFit) tolerances, annihilating filters, and smoothed regularization parameter named as *sroi*.

To evaluate the performance of the algorithms for removing artifacts and preserving details, we use the Haar perceptual similarity index (HaarPSI) to calculate the similarity between the reference image and the reconstructed image [29].³ The HaarPSI ranges from 0 to 1, and higher values mean that the algorithm is better to reconstruct details of slice and remove artifacts.

The experiments will be carried out on real phantom and in vivo data to test different pMRI reconstruction algorithms. The phantom MR images are acquired on a 3T MRI System (Tim Trio, Siemens, Erlangen, Germany). A turbo spin-echo sequence was used to acquire T_2 -weighted images. The detailed imaging parameters are as follows: field of view

¹The code is available at <https://people.eecs.berkeley.edu/~mlustig/Software.html>.

²The code is available at <https://bispl.weebly.com/aloha-for-mr-recon.html>.

³The code is available at <http://www.math.uni-bremen.de/cda/HaarPSI/>.

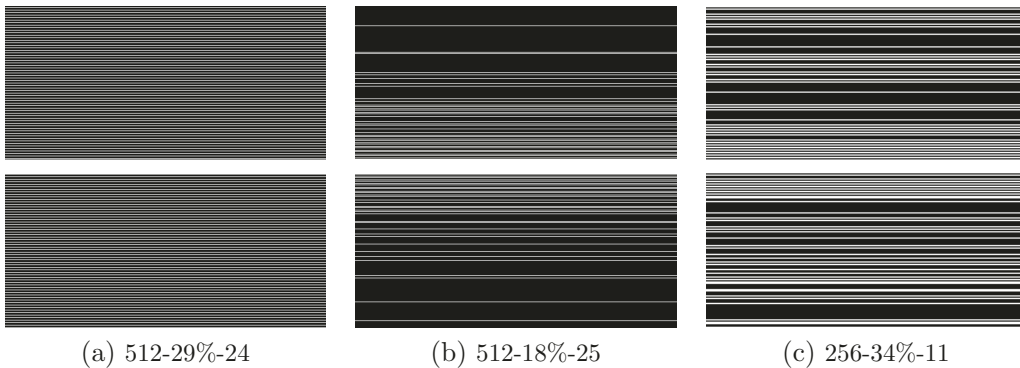


Figure 3. Sampling modes for the K -space. (a) 29% data by the uniform sampling model of 512×512 (one line taken from every four lines) with 24 ACS lines (the middle white area); (b) 18% data by the random sampling model of 512×512 with 25 ACS lines; (c) 34% data by the random sampling model of 256×256 with 11 ACS lines.

(FOV) = 256×256 mm 2 , image matrix size = 512×512 , slice thickness (ST) = 3 mm, flip angle = 180 degree, repetition time (TR) = 4000 ms, echo time (TE) = 71 ms, echo train length (ETL) = 11, and number of excitation (NEX) = 1.

4.3. Comparisons with other methods: MRI phantoms. In this subsection, three pMRI reconstruction methods—FADHFA [21], ℓ_1 -ESPIRiT [33], and ALOHA [15]—are compared with our proposed SENSE3d model on two slices of the MRI phantoms.

We first use four MRI phantom images under the 512×512 (512–29%–24) sampling model as shown in Figure 3(a), that is, the uniform sampling model of 512×512 with one line taken from every four lines and with 24 ACS lines. In Figure 4, panel (a) is the SoS image reconstructed from the full K -space data, while panel (b) is the SoS image with blurring and aliasing artifacts by four coil images from the downsampled K -space data by the uniform sampling mode in Figure 3(a). The regularization parameter λ is 0.035 and 0.001 for ℓ_1 -ESPIRiT and our SENSE3d model, respectively. The settings for ALOHA are four levels of pyramidal decomposition with decreasing LMaFit tolerances (0.3, 0.03, 0.003, 0.0003), annihilating filters with size of 11×11 , and $sroi = 10$.

The four pMRI reconstruction algorithms can retrieve most of the information from parts of the K -space data, but the images in Figure 4(c), (d) and (e) by ALOHA, FADHFA, and ℓ_1 -ESPIRiT, respectively, have some obvious aliasing artifacts, which are removed by our SENSE3d model and do not appear in Figure 4(f). That is to say, the correlated features by 3D tight framelet can be utilized to regularize the reconstruction image. We provide the zoomed-in parts of the reconstructed images in Figure 4(a')–(f') for distinguishing their difference. One can see that the ‘circle’ and ‘line’ false aliasing artifacts in Figure 4 (b') are mostly reduced by the regularized algorithms, but false ‘circle’ structures on the black region and noisy artifacts still appear in the zoomed-in image Figure 4(c') by low-rank regularization, while the ‘line’ artifact exists at the left-down corner of the zoomed-in image Figure 4(d') by the 2D-U model and at the middle of the zoomed-in image Figure 4(e') by ℓ_1 -ESPIRiT using 2D wavelet regularization without considering the correlated features of coil images. Figure 4(f'), by our

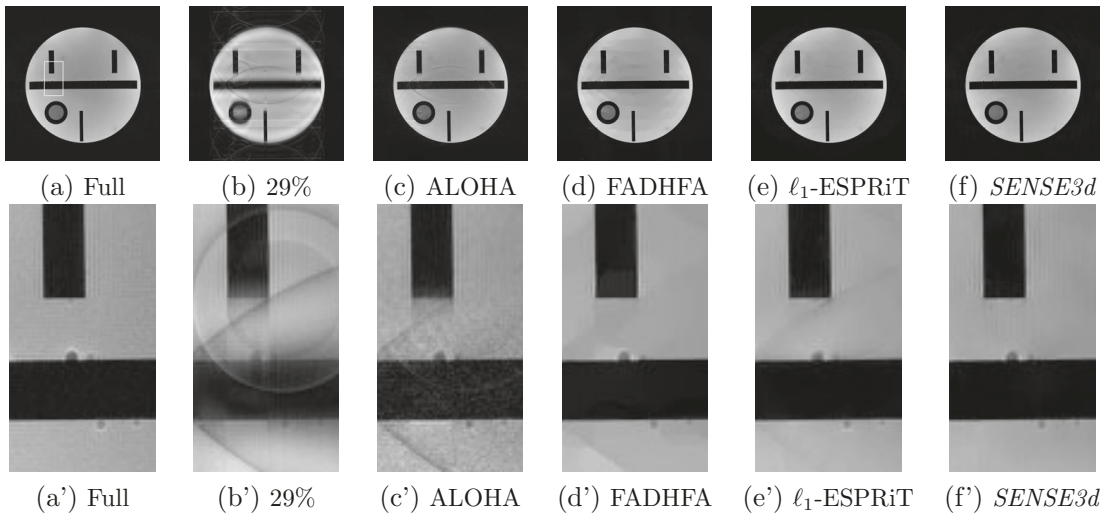


Figure 4. MRI phantoms of slice 1 with size 512×512 . (a) Reference SoS image by four full K -space data with zoomed-in area. (b) SoS image by four coil images by 29% K -space data on uniform sampling mode in Figure 3(a). (c) ALOHA. (d) FADHFA. (e) ℓ_1 -ESPIRiT. (f) Our proposed 3D-US model. (a')–(f') are the zoomed-in parts of (a)–(f), respectively.

Table 1

The HaarPSIs of the zoomed-in parts of reconstructed images by ALOHA, FADHFA, ℓ_1 -ESPIRiT, and SENSE3d in Algorithm 3.1 for removing artifacts and preserving details.

| Algorithm | ALOHA | FADHFA | ℓ_1 -ESPIRiT | SENSE3d |
|----------------------------|-------|--------|-------------------|-------------|
| Zoomed-in parts in figures | | | | |
| Figure 4 | 0.68 | 0.81 | 0.84 | 0.90 |
| Figure 5 | 0.73 | 0.85 | 0.86 | 0.92 |
| Figure 7 | | | | |
| First row | 0.89 | 0.93 | 0.95 | 0.96 |
| Second row | 0.87 | 0.90 | 0.93 | 0.96 |

SENSE3d model, does not have these aliasing artifacts, and it removes noise and preserves details of the edges closer to the reference image Figure 4(a') with full K -space data. The HaarPSIs in Table 1 of these four zoomed-in images by ALOHA, FADHFA, ℓ_1 -ESPIRiT, and SENSE3d are 0.68, 0.81, 0.84, and 0.90, respectively. Our SENSE3d algorithm can get the highest index, which means that our SENSE3d model can efficiently remove artifacts and preserve details.

We next use four MRI phantom images under the 512×512 (512–18%–25) sampling model as shown in Figure 3(b). That is, we use 18% sampling rate and 25 ACS lines to collect K -space data for this phantom slice. The parameter settings for ALOHA are four levels of pyramidal decomposition with decreasing LMaFit tolerances (0.3, 0.03, 0.003, 0.0003), 9×9 annihilating filters, and $sroi = 8$. The reconstructed results by ALOHA, FADHFA, ℓ_1 -ESPIRiT with regularization parameter $\lambda = 0.025$, and the proposed SENSE3d model with parameter $\lambda = 0.0002$ are shown in Figure 5(c), (d), (e), and (f), respectively.

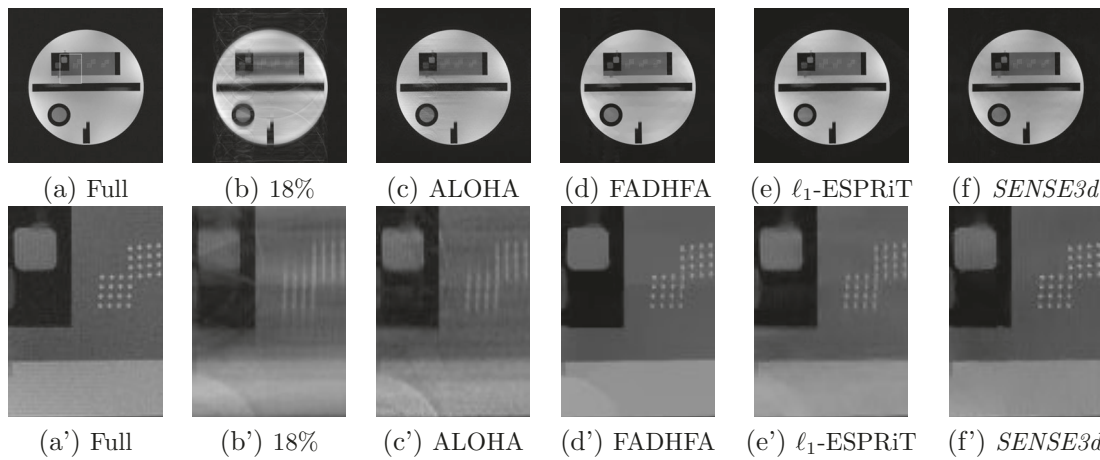


Figure 5. MRI phantoms of slice 2 with size 512×512 . (a) Reference SoS image by four full K -space data, (b) SoS image by 18% K -space data with sampling model in Figure 3(b). (c) ALOHA. (d) FADHFA. (e) ℓ_1 -ESPIRiT. (f) Our proposed SENSE3d model. (a')–(f') are the zoomed-in parts of (a)–(f), respectively.

Due to the downsampling operation on the K -space, the SoS image in Figure 5(b) from 18% K -space data is blurry and has lots of aliasing artifacts. The ALOHA, FADHFA, ℓ_1 -ESPIRiT, and proposed SENSE3d model can reconstruct most of details of the target slice and reduce aliasing with respect to reference image by full K -space data in Figure 5(c)–(f). However, Figure 5(c) by the ALOHA method has obvious aliasing artifacts and false structures, which is not suitable for doctor's diagnosis. We present the zoomed-in parts of the reconstruction images as Figure 5(a')–(f') to further compare these methods. It is obvious to see that our SENSE3d model can efficiently remove aliasing artifacts and keep the structures of the imaging slice. The ALOHA method is not efficient at preserving the shape of the bright ‘points’ and separating the boundary between the upper and lower regions and at aliasing artifacts in the zoomed-in images in Figure 5(c’); ℓ_1 -ESPIRiT is better than ALOHA at retrieving the bright ‘points’ and reducing aliasing artifacts, but it is worse than FADHFA and our SENSE3d model at preserving the boundary edges; the FADHFA model is almost the same as SENSE3d at preserving structural details of the slice, but Figure 5(d') by FADHFA has ‘arc’ artifacts at left-down of the zoomed-in image and false ‘gray’ edges covering the regions of bright ‘points’. Figure 5(e') by ℓ_1 -ESPIRiT also has the same aliasing artifact problem as that in Figure 5(d') by FADHFA, but it is not efficient at preserving sharp edges and blurs these regions. All the above issues in Figure 5(c')–(e') do not appear in Figure 5(f') by our SENSE3d model. The HaarPSIs in Table 1 of these four zoomed-in images by ALOHA, FADHFA, ℓ_1 -ESPIRiT, and SENSE3d are 0.73, 0.85, 0.86, and 0.92, respectively. It shows that our SENSE3d model gives the best performance for reconstructing the slice image.

The 3D tight framelet regularization is essentially different from the 2D tight framelet regularization when extracting the features of the correlated coil images for pMRI reconstruction. Our SENSE3d model not only has the merit of 2D tight framelet-based FADHFA to preserve details but also utilizes correlated features to remove aliasing artifacts caused by

the downsampling operation in K -space. This case again shows that our SENSE3d pMRI reconstruction algorithm can reconstruct most details of the slice and remove aliasing artifacts when the accelerated sampling rate is high.

4.4. Comparisons with other methods: In vivo data. In this subsection, we test our SENSE3d model on MRI data that were obtained by head examination from a healthy volunteer. The detailed imaging was done on a 3T MRI system. Transverse T_2 -weighted images were acquired with a turbo spin-echo sequence. The detail imaging parameters for Figure 7 are as follows: $\text{FOV} = 256 \times 256 \text{ mm}^2$, image matrix size = 256×256 , $\text{ST} = 3 \text{ mm}$, flip angle = 150 degree, $\text{TR} = 5920 \text{ ms}$, $\text{TE} = 101 \text{ ms}$, $\text{ETL} = 11$, and $\text{NEX} = 1$.

The MR signal of each slice is received by 32 channels, and the reference image of one slice in Figure 6(a) is an SoS image of 32 coil images by the full K -space data. In phase direction, about 34% of K -space data are collected using the pseudorandom sampling mode with 11 ACS lines in Figure 3(c). The resulting SoS image of the collected 34% K -space data in Figure 6(b) is noisy, and the brain structures are blurry. Furthermore, faint semicirclelike aliasing artifacts can be seen in the upper and lower portions of the image due to the accelerating K -space sampling mode.

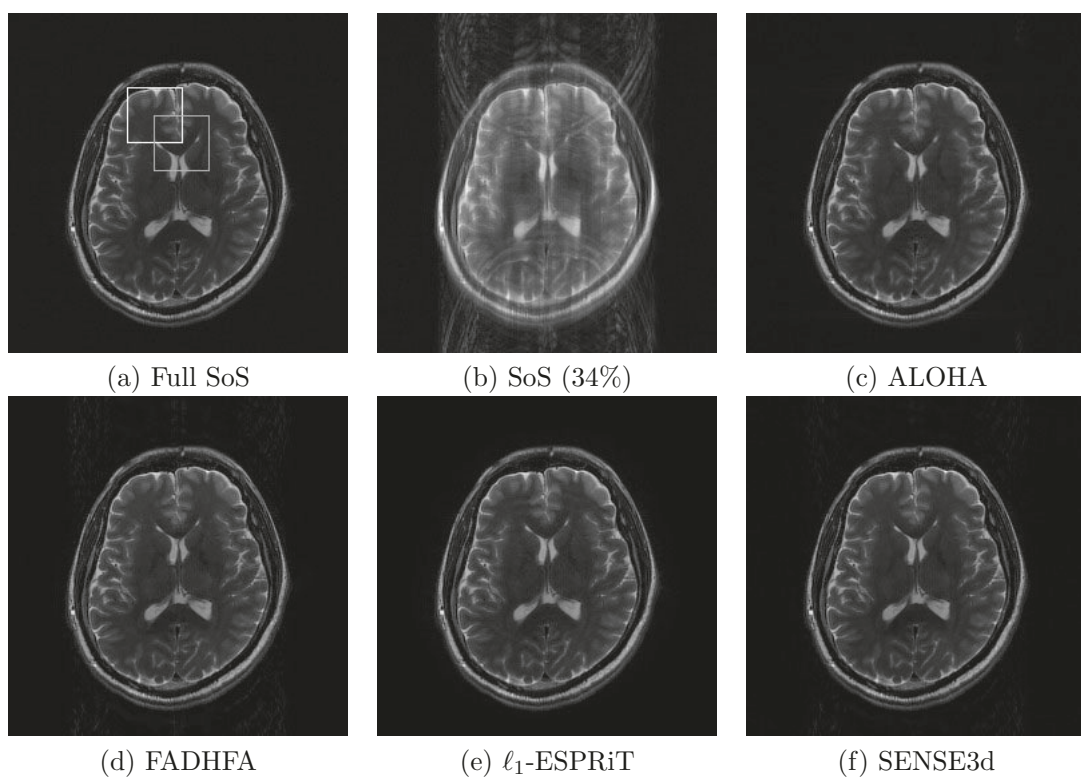


Figure 6. *In vivo* data with sampling model 256×256 ($256 - 34\% - 11$) as shown in Figure 3(c) with two to-be zoomed-in square areas. (a) Reference SoS image of 32 coil images by full K -space data with two zoomed-in regions. (b) SoS image by 34% K -space data. (c) ALOHA. (d) FADHFA. (e) ℓ_1 -ESPRiT. (f) Our SENSE3d model.

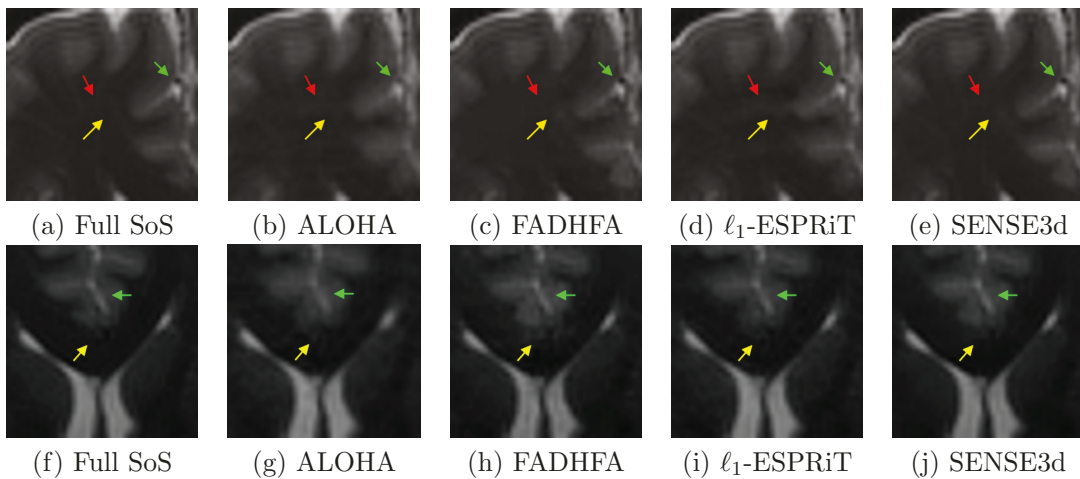


Figure 7. Two zoomed-in parts of Figure 6. (a) and (f) show reference SoS image. (b) and (g) show ALOHA results. (c) and (h) show FADHFA results. (d) and (i) show ℓ_1 -ESPIRiT results. (e) and (j) show our SENSE3d model results.

The reconstructions created by the ALOHA, FADHFA, ℓ_1 -ESPIRiT, and our SENSE3d models are shown in Figure 6(c), (d), (e), and (f), respectively. Their parameter settings are as follows: four levels of pyramidal decomposition with decreasing LMaFit tolerances ($10^{-1}, 10^{-2}, 10^{-3}, 10^{-4}$), 9×9 annihilating filters, and regularization parameter $sroi = 1.1$ for ALOHA; ℓ_1 -ESPIRiT with $\lambda = 0.003$; and our 3D SENSE3d algorithm with $\lambda = 0.00001$. Clearly, the quality of the images in Figure 6(c), (d), (e), and (f) is much better than the one in Figure 6(b) in terms of the structures of the slice, the levels of noise, and the aliasing artifacts.

To discriminate the difference of reconstructed images, we zoomed in on two square regions as in Figure 6(a) to compare the quality of the reconstructions by the ALOHA, FADHFA, ℓ_1 -ESPIRiT, and our SENSE3d models. The first region at the left side of frontal lobe is zoomed in on and provided in Figure 7(a)–(e). According to the HaarPSIs in Table 1, Figure 7(b)–(e) by ALOHA, FADHFA, ℓ_1 -ESPIRiT, and SENSE3d are 0.89, 0.93, 0.95, and 0.96, respectively. Our SENSE3d algorithm is the best to reconstruct slice details from *in vivo* data.

We label three positions by red, green, and yellow arrows to compare their differences by different algorithms. The artery pointed out by the green arrow in Figure 7(b) by ALOHA is not clear and is blurred, but the arterial structures in Figure 7(c), (d), and (e), respectively, by FADHFA, ℓ_1 -ESPIRiT, and SENSE3d are more obvious than that by ALOHA. The FADHFA and SENSE3d models are better than the ℓ_1 -ESPIRiT method and reconstruct the arterial structures almost identically to the reference one in Figure 7(a). At the region of white matter between the red arrow and the yellow arrow, there are aliasing artifacts in Figure 7(d) by ℓ_1 -ESPIRiT, extending from the frontal lobe into white matter; the boundary between the frontal lobe and white matter is blurry in Figure 7(b) by ALOHA; there are ‘white artifacts’ (yellow arrow pointing) in Figure 7(b) by FADHFA; but Figure 7(e), by our SENSE3d model, does not have these aliasing problems and provides an obvious boundary between tissues and is very close to the reference image in Figure 7(a).

We zoom in on another part of slice at the anterior border of the corpus callosum region and present zoomed-in images in Figure 7(f)–(j). The lobus images (green arrow) in Figure 7(h), (i) and (j), respectively, reconstructed by FADHFA, ℓ_1 -ESPIRiT, and our SENSE3d, still display better tissue structure than that in Figure 7(g) by ALOHA. The low-rank regularized method ALOHA does not preserve details in the tissue. The yellow arrow–pointing regions in Figure 7(g), (h) and (i), respectively, reconstructed by ALOHA, FADHFA, and ℓ_1 -ESPIRiT, have aliasing artifacts at the anterior border of the corpus callosum, which are false structures and do not appear in the reference image in Figure 7(f). However, in Figure 7(j), the aliasing artifact is removed by our SENSE3d model, and the geometry structure of the border is retrieved almost identically to the reference one. The HaarPSIs in Table 1 and Figure 7(f)–(i) by ALOHA, FADHFA, ℓ_1 -ESPIRiT, and SENSE3d are 0.87, 0.90, 0.93, and 0.96, respectively. The highest HaarPSI of our SENSE3d algorithm is consistent with our visual observation. The ALOHA, FADHFA, and ℓ_1 -ESPIRiT methods are not very efficient at removing these artifacts shown in Figure 6(b), but our SENSE3d model can be efficient at removing these aliasing artifacts, and its reconstructed structures of tissues are close to the reference image in Figure 6(a). That is to say, the 3D tight framelet–based SENSE3d algorithm has a greater capacity of preserving edges and reducing most of the aliasing artifacts caused by the downsampling operation in K -space than the 2D tight framelet–based, 2D wavelet-based, and low-rank–based regularization algorithms.

4.5. Comparisons with deep learning methods: Knee data. In this section, we compare our SENSE3d model with the deep learning model VarNet [32],⁴ which is built upon the fastMRI-UNet model [45] with a fastMRI data set.⁵

A set of knee with full K -space data from the fastMRI data set is used for this section. This knee data set was acquired using a clinical 1.5T system with a 2D turbo spin-echo sequence and a conventional Cartesian 2D TSE protocol. The detailed imaging parameters are as follows: $\text{FOV} = 280.00 \times 162.82 \times 4.50 \text{ mm}^3$, image matrix size = 640×372 , $\text{ST} = 4.5 \text{ mm}$, flip angle = 140 degree, $\text{TR} = 2800 \text{ ms}$, $\text{TE} = 32 \text{ ms}$, and $\text{ETL} = 4$. VarNet crops the reconstructed images from the network outputs with size 640×372 to be image blocks with size 320×320 centered on the original ones. We follow the settings of the VarNet model. The fully sampled images and reconstructed images by SENSE3d are also taken out from the same region for comparisons. Note that this knee data set serves as a validation set for the VarNet model in training process. Hence, there is no doubt that the trained model VarNet gives superior performance on such data than the fastMRI-UNet model.

The reference image in Figure 9(a) is an SoS image by 15 coil images with full K -space data. In phase direction, about 35% K -space data are collected using the pseudorandom sampling mode with 30 ACS lines in Figure 8(a). The resulting SoS image of the collected 35% K -space data in Figure 9(b) is noisy, and the knee structures are blurry. Furthermore, numerous faint elongated aliasing artifacts can be seen across the entire image due to the accelerating K -space sampling mode. The reconstructions by the VarNet and our SENSE3d model are shown in

⁴The code is available at https://github.com/facebookresearch/fastMRI/tree/main/fastmri_examples/varnet.

⁵The data set is available at <https://fastmri.med.nyu.edu/> and served as the baseline model for the 2020 fastMRI challenge [26].

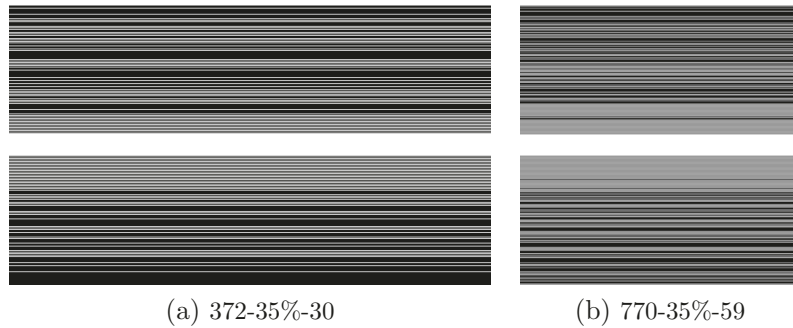


Figure 8. Sampling modes for the K -space. (a) 35% data by the uniform sampling model of 372×640 with 30 ACS lines; (b) 35% data by the random sampling model of 770×768 with 59 ACS lines.

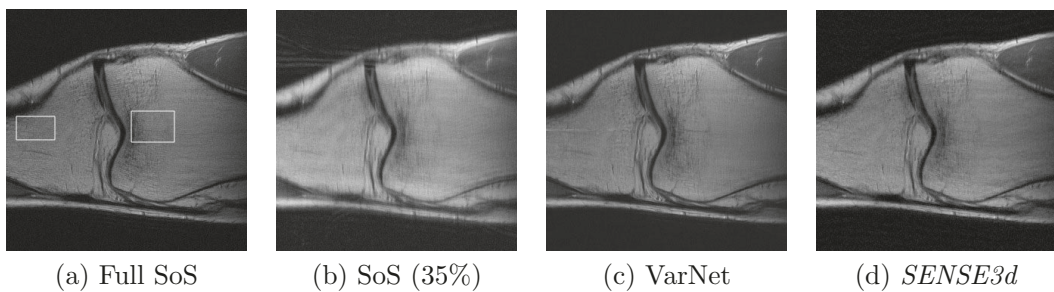


Figure 9. FastMRI data with sampling model $372 - 35\% - 30$ as shown in Figure 8(a) with two to-be zoomed-in rectangle areas. (a) Reference SoS image of 15 coil images by full K -space data with two zoomed-in regions. (b) SoS image by 35% K -space data. (c) VarNet. (d) Our SENSE3d model.

Figure 9(c) and (d), respectively. The parameter setting of our 3D SENSE3d algorithm is $\lambda = 0.0005$, which remains the same throughout the subsequent experiments. Clearly, the quality of the images in Figure 9(c) and (d) is much better than the one in Figure 9(b) in terms of the structures of the slice, the levels of noise, and the aliasing artifacts. To compare the difference between these two reconstructed images, we zoomed in on parts of the femur and tibia regions and show them in Figure 10. It is obvious that the zoomed-in images by VarNet are smoother than the original ones (loss of details) and have some aliasing artifacts, such as the tibia image with a ‘white line’ and the femur image with a ‘black line.’ But our SENSE3d algorithm can suppress these artifacts, and its reconstructed images have structures closer to the reference one. We provide their HaarPSIs for further comparisons. The HaarPSIs provided in Table 2 for the tibia and femur images in Figure 10(c) and (f) by our SENSE3d model are 0.891 and 0.894, respectively, but the HaarPSIs by VarNet in Figure 10(b) and (e) are 0.866 and 0.879, respectively. Our SENSE3d model gets higher HaarPSIs than VarNet does. Another knee data set is different from the data used in FastMRI, which are provided at an MRI data website.⁶ This knee data set was acquired using a clinical 2.89T system with a turbo spin-echo sequence. The detail imaging parameters are as follows: $\text{FOV} = 280 \times 280.7 \times 4.5$

⁶<http://www.mridata.org>.

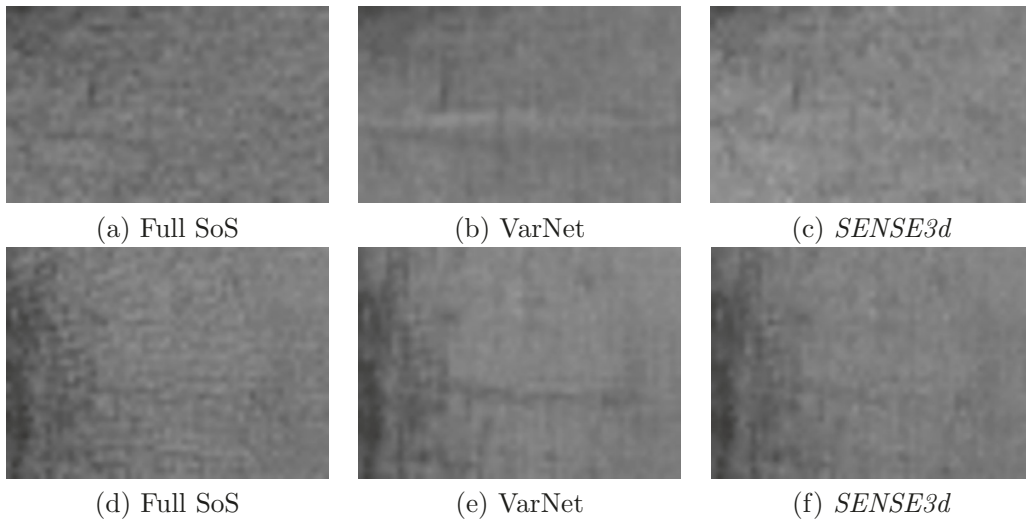


Figure 10. Two zoomed-in parts of Figure 9. (a) and (d) show reference SoS image. (b) and (e) show VarNet results. (c) and (f) show our SENSE3d model results.

Table 2

The HaarPSIs of the zoomed-in parts of reconstructed images by VarNet, fastMRI-UNet, and SENSE3d in Algorithm 3.1 for removing artifacts and preserving details.

| Algorithm | Figure 10 | | Algorithm | Figure 12 | |
|-----------|--------------|--------------|--------------|--------------|--------------|
| | First row | Second row | | First row | Second row |
| VarNet | 0.866 | 0.879 | fastMRI-UNet | 0.906 | 0.836 |
| SENSE3d | 0.891 | 0.894 | SENSE3d | 0.970 | 0.961 |

mm³, image matrix size = 768 × 770, slice thicknesses = 4.5 mm, flip angle = 150 degree, TR = 2800 ms, and TE = 22 ms.

We attempt to use VarNet to reconstruct the MRI image on these new knee data. However, VarNet cannot produce correct results on the new knee data. The main reason is due to the inaccurate sensitivity maps estimated by VarNet, besides the common generalization limitations of the network model such as inconsistent images from the fastMRI data set, different machines' data acquisition settings, and so on. We hence use another model, fastMRI-UNet [45], that has fewer restrictions to reconstruct the result and compare it with our model. Unlike VarNet, fastMRI-UNet directly takes K -space data as input and produces reconstructed MRI images without the need for a sensitivity map estimation model. The source code of fastMRI-UNet is available at the GitHub website.⁷

We use the sampling mode with 59 ACS lines in Figure 8(b) to collect 35% K -space data for the fastMRI-UNet and our SENSE3d model to reconstruct the target image. The reconstructions by fastMRI-UNet and our SENSE3d model are shown in Figure 11(c) and (d), respectively. The SoS image in Figure 11(b) by the collected 35% K -space data is blurry, but

⁷The code is available at https://github.com/facebookresearch/fastMRI/tree/main/fastmri_examples/unet.

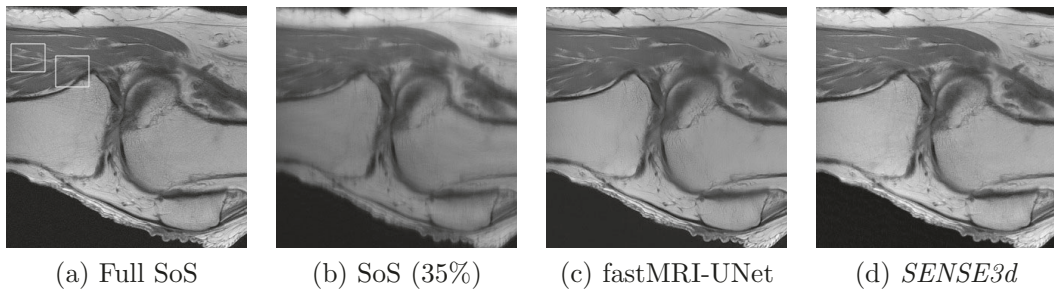


Figure 11. MRI data with sampling model 770 – 35%-59 as shown in Figure 8(b) with two to-be zoomed-in rectangle areas. (a) Reference SoS image of 15 coil images by full K -space data with two zoomed-in regions. (b) SoS image by 35% K -space data. (c) fastMRI-UNet. (d) Our SENSE3d model.

reconstructed images by fastMRI-UNet and our SENSE3d model are clear with more structure details. To compare the difference between Figure 11(c) and (d), we zoomed in on parts of the popliteus and soleus muscle regions and show them in Figure 10. The reconstructed images by our SENSE3d model have clearer organizational details than the images reconstructed by fastMRI-UNet. The popliteus part, by our model, is almost close to reference one with HaarPSI value 0.961 (see Table 2), but the image by fastMRI-UNet is only 0.836. The HaarPSI values of another part of the soleus muscle by fastMRI-UNet and our SENSE3d model are 0.906 and 0.970, respectively. Our model achieves a 0.064 higher result than the fastMRI-UNet model. This case shows that our model is stable for reconstructing images and gets good results from the different data by different machine acquisition.

5. Conclusions and further remarks. We have proposed an effective SENSE3d model for the pMRI reconstruction. The proposed method can reconstruct high-quality images from the sampled K -space data with a high acceleration rate by decoupling effects of the desired image (slice) and sensitivity maps. The developed SENSE3d algorithm, which consists of a sequence of alternating slice steps and sensitivity steps, exploits the decoupled slices and sensitivity maps. Each slice step solves a convex optimization problem for an estimated image with the given estimations of sensitivity maps, while each sensitivity step solves a nonconvex optimization problem for estimated sensitivity maps with the given estimation of the desired image. The convergence analysis for the optimization algorithm in both the slice step and sensitivity step has been studied. Numerical results on various data and comparisons to other state-of-the-art methods, including deep learning methods, have demonstrated that the proposed method can produce images of high quality and efficiently reduce aliasing artifacts caused by inaccurate estimation of each coil sensitivity.

The use of neural networks is to learn the relationship between input data (K -space data) and output data (for example, slice images) by training data. Thus, databases with a large amount of multicoil K -space data are needed to train the neural networks for pMRI reconstruction [18]. The challenge of pMRI reconstruction by using neural networks is their instability of predicting output data when the imaging conditions of input data are different with different training conditions [35]. How to take the advantages of our model to improve the performance of the models based on deep learning methods can be one of our future research topics.

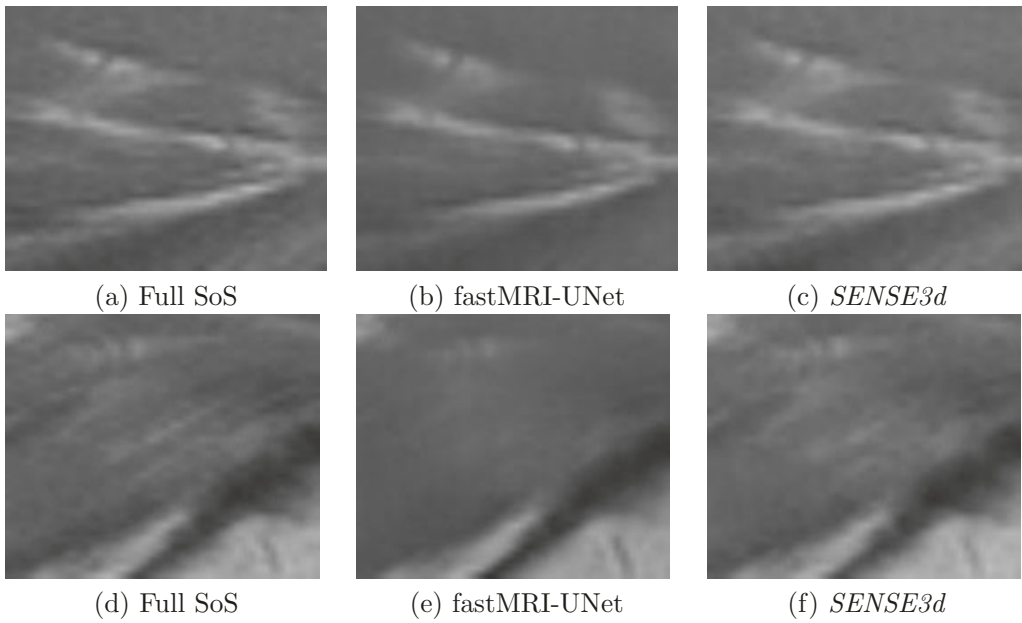


Figure 12. Two zoomed-in parts of Figure 11. (a) and (d) show reference SoS image. (b) and (e) show fastMRI-UNet reconstruction. (c) and (f) show SENSE3d reconstruction.

Appendix A.

A.1. Proof of Theorem 3.1. In this appendix, we give the proof of Theorem 3.1. To this end, we first introduce our notation and recall some necessary background materials from optimization. The class of all lower semicontinuous convex functions $f : \mathbb{C}^d \rightarrow (-\infty, +\infty]$ such that $\text{dom } f := \{x \in \mathbb{C}^d : f(x) < +\infty\} \neq \emptyset$ is denoted by $\Gamma_0(\mathbb{C}^d)$. The indicator function of a closed convex set C in \mathbb{C}^d is defined, at $u \in \mathbb{C}^d$, as

$$\iota_C(u) := \begin{cases} 0 & \text{if } u \in C, \\ +\infty, & \text{otherwise.} \end{cases}$$

Clearly, the indicator function ι_C is in $\Gamma_0(\mathbb{C}^d)$ for any closed nonempty convex set C .

For a function $f \in \Gamma_0(\mathbb{C}^d)$, the proximity operator of f with parameter λ , denoted by $\text{prox}_{\lambda f}$, is a mapping from \mathbb{C}^d to itself, defined for a given point $x \in \mathbb{C}^d$ by

$$\text{prox}_{\lambda f}(x) := \underset{u \in \mathbb{C}^d}{\text{argmin}} \left\{ \frac{1}{2} \|u - x\|_2^2 + \lambda f(u) \right\}.$$

We also need the notation of the conjugate. The conjugate of $f \in \Gamma_0(\mathbb{C}^d)$ is the function $f^* \in \Gamma_0(\mathbb{C}^d)$ defined at $x \in \mathbb{C}^d$ by $f^*(x) := \sup\{\langle u, x \rangle - f(u) : u \in \mathbb{C}^d\}$. A key property of the proximity operators of f and its conjugate is

$$(A.1) \quad \text{prox}_{\lambda f}(x) + \lambda \text{prox}_{\lambda^{-1} f^*}(x/\lambda) = x,$$

which holds for all $x \in \mathbb{C}^n$ and any $\lambda > 0$.

For a real function f defined on \mathbb{C}^d , we say that f is Fréchet differentiable at $x \in \mathbb{C}^d$ if there exists a $v \in \mathbb{C}^d$ such that

$$\lim_{y \rightarrow x} \frac{|f(y) - f(x) - \langle v, y - x \rangle|}{\|y - x\|_2} = 0.$$

The vector v is called the gradient of f at x , denoted by $\nabla f(x)$. As an example, $\nabla(\|A \cdot -b\|_2^2) = A^\top(A \cdot -b)$, where $A \in \mathbb{C}^{d \times n}$ and $b \in \mathbb{C}^d$.

We consider the following optimization problem

$$(A.2) \quad \min_{x \in \mathbb{C}^n} p(x) + q(x) + r(Ax),$$

where A is a $d \times n$ matrix, $p \in \Gamma_0(\mathbb{C}^n)$ is differentiable, $q \in \Gamma_0(\mathbb{C}^n)$, and $r \in \Gamma_0(\mathbb{C}^d)$.

Several algorithms have been developed for the optimization problem (A.2); see, for example, [20, 39]. We adopt the algorithm given in [39] for problem (A.2) since it converges under a weaker condition and can choose a larger step-size, yielding a faster convergence. This algorithm, named PD3O, has the following iteration:

$$(A.3a) \quad x^k = \text{prox}_{\gamma q}(y^k),$$

$$(A.3b) \quad z^{k+1} = \text{prox}_{\delta r^*} \left((I - \gamma \delta A A^\top) z^k + \delta A (2x^k - y^k - \gamma \nabla p(x^k)) \right),$$

$$(A.3c) \quad y^{k+1} = x^k - \gamma \nabla p(x^k) - \gamma A^\top z^{k+1}.$$

One PD3O iteration can be viewed as an operator T_{PD3O} such that $(y^{k+1}, z^{k+1}) = T_{\text{PD3O}}(y^k, z^k)$. The convergence analysis of PD3O is given in the following lemma.

Lemma A.1 (sublinear convergence rate [39]). *Let $p \in \Gamma_0(\mathbb{C}^n)$, and let its gradient be Lipschitz continuous with constant ν . Choose γ and δ such that $\gamma < 2/\nu$ and $B = \frac{\gamma}{\delta}(I - \gamma \delta A A^\top)$ is positive definite. Let (y^*, z^*) be any fixed point of T_{PD3O} , and let $\{(y^k, z^k)\}_{k \geq 0}$ be the sequence generated by PD3O. Define $\|(y, z)\|_B := \sqrt{\|y\|^2 + \langle z, Bz \rangle}$. Then, the following statements hold.*

- (i) *The sequence $\{(\|y^k, z^k\|_B - (y^*, z^*)\|_B)\}_{k \geq 0}$ is monotonically nonincreasing.*
- (ii) *The sequence $\{(\|y^{k+1}, z^{k+1}\|_B - (y^k, z^k)\|_B\}_{k \geq 0}$ is monotonically nonincreasing. Moreover,*

$$\|(y^{k+1}, z^{k+1}) - (y^k, z^k)\|_B^2 = o\left(\frac{1}{k+1}\right).$$

We remark that the statements in Lemma A.1 are originally presented in real vector space \mathbb{R}^n (see [39]). By using the inner product (3.1) for \mathbb{C}^n , we essentially work with real vector space \mathbb{R}^{2n} . Therefore, the results in Lemma A.1 hold on \mathbb{C}^n as well.

By identifying p , q , r , and A in (A.2), respectively, as

$$(A.4) \quad p(\cdot) = \frac{1}{2} \|M \cdot -g\|^2, \quad q(\cdot) = \iota_{\mathbb{R}^n}(\cdot), \quad r(\cdot) = \|\Gamma(\cdot + b)\|_1, \quad A = WN$$

with $b = W(I_L \otimes F^{-1})g$, the PD3O algorithm can be applied for solving problem (3.3). To efficiently implement this algorithm, we need to know both prox_q and $\text{prox}_{\delta r^*}$. By the definition of the proximity operator, $\text{prox}_q = \text{Re}$; i.e., prox_q takes the real part of an input. The proximity operator $\text{prox}_{\delta r^*}$ is given in the next lemma.

Lemma A.2. *Let r be given in (A.4). Then, for $\delta > 0$ and $z \in \mathbb{C}^d$, $\text{prox}_{\delta r^*}(z) = (z + \delta b) - \text{prox}_{\|\Gamma\|_1}(z + \delta b)$.*

Proof. Write $w = \text{prox}_{\delta r^*}(z)$. From the identity (A.1), $w = z - \delta \text{prox}_{\delta^{-1}r}(\delta^{-1}z)$. Based on the separable property of r in (A.4)—that is, $r(u) = \|\Gamma(u + b)\|_1 = \sum_{k=1}^d \gamma[k]|u[k] + b[k]|$ —we have that $w[k] = z[k] - \delta \text{prox}_{\delta^{-1}\gamma[k] \cdot + b[k]}(\delta^{-1}z[k])$, for $k = 1, 2, \dots, d$. By a simple manipulation on the above proximity operator, we have that $w[k] = (z[k] + \delta b[k]) - \text{prox}_{\gamma[k] \cdot |}(z[k] + \delta b[k])$. This completes the proof of this result. \blacksquare

The proximity operator $\text{prox}_{\|\Gamma\|_1}$ is the well-known soft shrinkage operator $\text{soft}(x, \Gamma)$. To show the convergence of the PD3O algorithm under the proper choices of parameters γ and δ , we need the following lemma.

Lemma A.3. *Let M and g be given in (1.2), and let p and A be given in (A.4). Then, the following statements hold:*

- (i). *The gradient of p is κ -Lipschitz continuous, where κ is given in (3.4).*
- (ii). *For any positive numbers γ and δ , the matrix $I - \gamma\delta AA^\top$ is positive definite if and only if $\gamma\delta < 1/\kappa$.*

Proof. Item (i): Note that $\nabla p(u) = M^\top(Mu - g)$. Then, ∇p is $\|M\|^2$ -Lipschitz continuous. Define $Q = \sum_{\ell=1}^L s_\ell s_\ell^\top$, which is the entrywise conjugate of the matrix $\sum_{\ell=1}^L s_\ell s_\ell^\top$. From (1.2), we have $M^\top M = \sum_{\ell=1}^L \text{diag}(\bar{s}_\ell) F^\top P F S_\ell = (F^\top P F) \odot Q$. Since Q is a positive semidefinite matrix, we have, for example, by Theorem 5.5.18 in [13], that $\|M^\top M\|_2 \leq \max_{i,j} |Q[i,j]| \|F^\top P F\|_2$. Furthermore, due to $\|F^\top P F\| \leq 1$, $\max_{i,j} |Q[i,j]| = \max_k |Q[k,k]|$, and $Q[k,k] = \sum_{\ell=1}^L |s_\ell[k]|^2$, we have $\|M^\top M\|_2 \leq \kappa$.

Item (ii): The proof replies on the estimation of the norm of AA^\top . From $A = WN$ and $W^\top W = I$, one has $\|AA^\top\|_2 = \|A^\top A\|_2 = \|N^\top N\|_2$. Similar to the discussion in item (i), we have $N^\top N = (F^\top(I - P)F) \odot Q$ and $\|N^\top N\|_2 \leq \kappa$. Therefore, the largest eigenvalue of AA^\top is less than κ . As a result, $I - \gamma\delta AA^\top$ is positive definite if and only if $\gamma\delta < 1/\kappa$. This completes the proof. \blacksquare

Proof of Theorem 3.1. By Lemma A.3, the gradient p in (A.4) is κ -Lipschitz continuous and the matrix B is positive definite if and only if $\gamma\delta < 1/\kappa$; the result of this theorem follows immediately from Lemma A.1. \blacksquare

A.2. Proof of Theorem 3.2. For given P_{sel} , M , g_{est} , Γ , and W in (3.10), define

$$(A.5) \quad h(s) := \frac{1}{2} \|P_{\text{sel}}(Qs - g_{\text{est}})\|_2^2 + \frac{1}{2} \|\Gamma W s\|_2^2.$$

We have the following result for the function h .

Lemma A.4. *Let h be defined in (A.5). Then, the gradient of h is Lipschitz continuous with Lipschitz constant $\|u\|_\infty^2 + \|\text{diag}(\Gamma)\|_\infty^2$.*

Proof. Note that $\nabla h(s) = Q^\top P_{sel}(Qs - g_{est}) + W^\top \Gamma^2 W s$. For any vectors s_1 and s_2 , we have $\|\nabla h(s_1) - \nabla h(s_2)\|_2 = \|(Q^\top P_{sel}Q + W^\top \Gamma^2 W)(s_1 - s_2)\|_2 \leq (\|Q\|_2^2 \|P_{sel}\|_2 + \|W\|_2^2 \|\Gamma\|_2^2) \|s_1 - s_2\|_2$. We know that $\|P_{sel}\|_2 = 1$, $\|W^\top\|_2 = 1$, and $\|\Gamma\|_2 = \|\text{diag}(\Gamma)\|_\infty$. Next, we estimate the norm of Q . Since

$$\begin{aligned} Q^\top Q &= (I_L \otimes (F\text{diag}(u)))^\top (I_L \otimes (F\text{diag}(u))) \\ &= (I_L \otimes (\text{diag}(u)F^{-1}))(I_L \otimes (F\text{diag}(u))) \\ &= I_L \otimes (\text{diag}(u)\text{diag}(u)), \end{aligned}$$

we have that $\|Q\|_2^2 = \|Q^\top Q\|_2 = \|I_L \otimes (\text{diag}(u)\text{diag}(u))\|_2 = \|\text{diag}(u)\|_2^2 = \|u\|_\infty^2$. Hence, the gradient of h is Lipschitz continuous with Lipschitz constant $\|u\|_\infty^2 + \|\text{diag}(\Gamma)\|_\infty^2$. \blacksquare

Proof of Theorem 3.2. Note that $h(s)$ is a quadratic polynomial with respect to s and the set D given in (3.9) is determined by a set of polynomials. Then, $h(s) + \iota_D(s)$ is a Kurdyka–Łojasiewicz function (see, e.g., [1]). Hence, the result is the direct consequence of Theorem 5.3 of [1]. \blacksquare

REFERENCES

- [1] H. ATTOUCH, J. BOLTE, AND B. SVAITER, *Convergence of descent methods for semi-algebraic and tame problems: Proximal algorithms, forward-backward splitting, and regularized Gauss–Seidel methods*, Math. Program. Ser. A, 137 (2013), pp. 91–129.
- [2] M. BLAIMER, F. BREUER, M. MUELLER, R. M. HEIDEMANN, M. A. GRISWOLD, AND P. M. JAKOB, *SMASH, SENSE, PILS, GRAPPA: How to choose the optimal method*, Top. Magn. Reson. Imag., 15 (2004), pp. 223–236.
- [3] J.-F. CAI, J. K. CHOI, AND K. WEI, *Data driven tight frame for compressed sensing MRI reconstruction via off-the-grid regularization*, SIAM J. Imaging Sci., 13 (2020), pp. 1272–1301.
- [4] L. CHAĀRI, J. C. PESQUET, A. BENAZZA-BENYAHIA, AND P. CIUCIU, *A wavelet-based regularized reconstruction algorithm for SENSE parallel MRI with applications to neuroimaging*, Med. Image Anal., 12 (2011), pp. 185–201.
- [5] I. Y. CHUN, B. ADCOCK, AND T. M. TALAVAGE, *Efficient compressed sensing SENSE pMRI reconstruction with joint sparsity promotion*, IEEE Trans. Med. Imaging, 35 (2016), pp. 354–368.
- [6] M. DONEVA, *Mathematical models for magnetic resonance imaging reconstruction: An overview of the approaches, problems, and future research areas*, IEEE Signal Process. Mag., 37 (2020), pp. 24–32.
- [7] W. A. EDELSTEIN, J. M. HUTCHISON, G. JOHNSON, AND T. REDPATH, *Spin warp NMR imaging and applications to human whole-body imaging*, Phys. Med. Biol., 25 (1980), 751.
- [8] S. G. FINLAYSON, J. D. BOWERS, J. ITO, J. L. ZITTRAIN, A. L. BEAM, AND I. S. KOHANE, *Adversarial attacks on medical machine learning*, Science, 363 (2019), pp. 1287–1289.
- [9] M. A. GRISWOLD, P. M. JAKOB, R. M. HEIDEMANN, M. NITTKA, V. JELLUS, J. WANG, B. KIEFER, AND A. HAASE, *Generalized autocalibrating partially parallel acquisitions (GRAPPA)*, Magn. Reson. Med., 47 (2002), pp. 1202–1210.
- [10] J. P. HALDAR AND J. ZHUO, *P-LORAKS: Low-rank modeling of local K-space neighborhoods with parallel imaging data*, Magn. Reson. Med., 75 (2016), pp. 1499–1514.
- [11] B. HAN, *Framelets and Wavelets: Algorithms, Analysis, and Applications*, Appl. Numer. Harmon. Anal., Springer, Cham, 2018.
- [12] B. HAN, T. LI, AND X. ZHUANG, *Directional compactly supported box spline tight framelets with simple geometric structure*, Appl. Math. Lett., 91 (2019), pp. 213–219.
- [13] R. HORN AND C. JOHNSON, *Topics in Matrix Analysis*, Cambridge University Press, Cambridge, UK, 1991.
- [14] M. JACOB, M. P. MANI, AND J. C. YE, *Structured low-rank algorithms: Theory, magnetic resonance applications, and links to machine learning*, IEEE Signal Process. Mag., 37 (2020), pp. 54–68.

[15] K. H. JIN, D. LEE, AND J. C. YE, *A general framework for compressed sensing and parallel MRI using annihilating filter based low-rank Hankel matrix*, IEEE Trans. Comput. Imaging, 2 (2016), pp. 480–495.

[16] K. H. JIN, M. T. MCCANN, E. FROUSTEY, AND M. UNSER, *Deep convolutional neural network for inverse problems in imaging*, IEEE Trans. Image Process., 26 (2017), pp. 4509–4522.

[17] F. KNOLL, C. CLASON, K. BREDIES, M. UECKER, AND R. STOLLBERGER, *Parallel imaging with nonlinear reconstruction using variational penalties*, Magn. Reson. Med., 67 (2012), pp. 34–41.

[18] F. KNOLL, K. HAMMERNIK, C. ZHANG, S. MOELLER, T. POCK, D. K. SODICKSON, AND M. AKCAKAYA, *Deep-learning methods for parallel magnetic resonance image reconstruction: A survey of the current approaches, trends, and issues*, IEEE Signal Process. Mag., 37 (2020), pp. 128–140.

[19] J. LI, H. FENG, AND X. ZHUANG, *Convolutional neural networks for spherical signal processing via area-regular spherical Haar tight framelets*, IEEE Trans. Neural Netw. Learn. Syst., (2022), doi: [10.1109/TNNLS.2022.3160169](https://doi.org/10.1109/TNNLS.2022.3160169).

[20] Q. LI AND N. ZHANG, *Fast proximity-gradient algorithms for structured convex optimization problems*, Appl. Comput. Harmon. Anal., 41 (2016), pp. 491–517.

[21] Y.-R. LI, R. H. CHAN, L. SHEN, Y.-C. HSU, AND W.-Y. I. TSENG, *An adaptive directional Haar framelet-based reconstruction algorithm for parallel magnetic resonance imaging*, SIAM J. Imaging Sci., 9 (2016), pp. 794–821.

[22] Y.-R. LI, L. SHEN, AND X. ZHUANG, *A tailor-made 3-dimensional directional Haar semi-tight framelet for pMRI reconstruction*, Appl. Comput. Harmon. Anal., 60 (2022), pp. 446–470.

[23] Y.-R. LI AND X. ZHUANG, *Parallel magnetic resonance imaging reconstruction algorithm by 3-dimension directional Haar tight framelet regularization*, in SPIE Proc. 11138, San Diego, 2019, pp. 111381C–1–8.

[24] M. LUSTIG AND J. M. PAULY, *SPIRiT: Iterative self-consistent parallel imaging reconstruction from arbitrary K -space*, Magn. Reson. Med., 64 (2010), pp. 457–471.

[25] J. LYU, U. NAKARMI, D. LIANG, J. SHENG, AND L. YING, *Kernl: Kernel-based nonlinear approach to parallel MRI reconstruction*, IEEE Trans. Med. Imaging, 38 (2019), pp. 312–321.

[26] M. J. MUCKLEY, B. RIEMENSCHNEIDER, A. RADMANESH, S. KIM, G. JEONG, J. KO, Y. JUN, H. SHIN, D. HWANG, M. MOSTAPHA, S. ARBERET, D. NICKEL, Z. RAMZI, P. CIUCIU, J.-L. STARCK, J. TEUWEN, D. KARKALOUSOS, C. ZHANG, A. SRIRAM, Z. HUANG, N. YAKUBOVA, Y. W. LUI, AND F. KNOLL, *Results of the 2020 fastMRI challenge for machine learning MR image reconstruction*, IEEE Trans. Med. Imaging, 40 (2021), pp. 2306–2317.

[27] M. MURPHY, M. ALLEY, J. DEMMEL, K. KEUTZER, S. VASANAWALA, AND M. LUSTIG, *Fast ℓ_1 -SPIRiT compressed sensing parallel imaging MRI: Scalable parallel implementation and clinically feasible run-time*, IEEE Trans. Med. Imaging, 31 (2012), pp. 1250–1262.

[28] K. P. PRUESSMANN, M. WEIGER, M. B. SCHEIDECKER, AND P. BOESIGER, *SENSE: Sensitivity encoding for fast MRI*, Magn. Reson. Med., 42 (1999), pp. 952–962.

[29] G. K. RAFAEL REISENHOFER, S. BOSSE, AND T. WIEGAND, *A Haar wavelet-based perceptual similarity index for image quality assessment*, Signal Process. Image Commun., 61 (2018), pp. 33–43.

[30] O. RONNEBERGER, P. FISCHER, AND T. BROX, *U-net: Convolutional networks for biomedical image segmentation*, in Medical Image Computing and Computer-Assisted Intervention—MICCAI 2015: 18th International Conference, Munich, Germany, October 5–9, 2015, Proceedings, Part III 18, Springer, 2015, pp. 234–241.

[31] P. J. SHIN, P. E. Z. LARSON, M. A. OHLIGER, M. ELAD, J. M. PAULY, D. B. VIGNERON, AND M. LUSTIG, *Calibrationless parallel imaging reconstruction based on structured low-rank matrix completion*, Magn. Reson. Med., 725 (2014), pp. 959–970.

[32] A. SRIRAM, J. ZBONTAR, T. MURRELL, A. DEFazio, C. L. ZITNICK, N. YAKUBOVA, F. KNOLL, AND P. JOHNSON, *End-to-end variational networks for accelerated MRI reconstruction*, in Medical Image Computing and Computer Assisted Intervention—MICCAI 2020: 23rd International Conference, Lima, Peru, October 4–8, 2020, Proceedings, Part II 23, Springer, 2020, pp. 64–73.

[33] M. UECKER, P. LAI, M. J. MURPHY, P. VIRTUE, M. ELAD, J. M. PAULY, S. S. VASANAWALA, AND M. LUSTIG, *ESPIRiT—an eigenvalue approach to autocalibrating parallel MRI: Where SENSE meets GRAPPA*, Magn. Reson. Med., 71 (2014), pp. 990–1001.

[34] M. UECKER AND M. LUSTIG, *Estimating absolute-phase maps using espirit and virtual conjugate coils*, Magn. Reson. Med., 77 (2017), pp. 1201–1207.

[35] C. P. B. A. V. ANTUN, F. RENNA, AND A. C. HANSEN, *On instabilities of deep learning in image reconstruction and the potential costs of AI*, Proc. Natl. Acad. Sci., 117 (2020), pp. 30088–30095.

[36] S. WANG, S. TAN, Y. GAO, Q. LIU, L. YING, T. XIAO, Y. LIU, X. LIU, H. ZHENG, AND D. LIANG, *Learning joint-sparse codes for calibration-free parallel MR imaging*, IEEE Trans. Med. Imaging, 37 (2018), pp. 251–261.

[37] D. S. WELLER, J. R. POLIMENI, L. GRADY, L. L. WALD, E. ADALSTEINSSON, AND V. K. GOYAL, *Sparsity-promoting calibration for GRAPPA accelerated parallel MRI reconstruction*, IEEE Trans. Med. Imaging, 32 (2013), pp. 1325–1335.

[38] Y. XIAO AND X. ZHUANG, *Adaptive directional Haar tight framelets on bounded domains for digraph signal representations*, J. Fourier Anal. Appl., 27 (2021), 7.

[39] M. YAN, *A new primal-dual algorithm for minimizing the sum of three functions with a linear operator*, J. Sci. Comput., 76 (2018), pp. 1698–1717.

[40] G. YANG, S. YU, H. DONG, G. SLABAUGH, P. L. DRAGOTTI, X. YE, F. LIU, S. ARRIDGE, J. KEEGAN, Y. GUO, AND D. FIRMIN, *Dagan: Deep de-aliasing generative adversarial networks for fast compressed sensing MRI reconstruction*, IEEE Trans. Med. Imaging, 37 (2017), pp. 1310–1321.

[41] Y. YANG, J. SUN, H. LI, AND Z. XU, *Deep ADMM-Net for compressive sensing MRI*, in Proceedings of the 30th International Conference on Neural Information Processing Systems, Curran Associates, 2016, pp. 10–18.

[42] M. YASHTINI, *Euler's elastica-based algorithm for parallel MRI reconstruction using SENsitivity encoding*, Optim. Lett., 14 (2020), pp. 1435–1458.

[43] X. YE, Y. CHEN, AND F. HUANG, *Computational acceleration for MR image reconstruction in partially parallel imaging*, IEEE Trans. Med. Imaging, 30 (2011), pp. 1055–1063.

[44] L. YING AND J. SHENG, *Joint image reconstruction and sensitivity estimation in SENSE (JSENSE)*, Magn. Reson. Med., 57 (2007), pp. 1196–1202.

[45] J. ZBONTAR, F. KNOLL, A. SRIRAM, T. MURRELL, Z. HUANG, M. J. MUCKLEY, A. DEFAZIO, R. STERN, P. JOHNSON, M. BRUNO, ET AL., *fastMRI: An Open Dataset and Benchmarks for Accelerated MRI*, preprint, [arXiv:1811.08839](https://arxiv.org/abs/1811.08839), 2018.